

JADES: The emergence and evolution of Ly α emission & constraints on the IGM neutral fraction

Gareth C. Jones^{1*}, Andrew J. Bunker¹, Aayush Saxena^{1,2}, Joris Witstok^{3,4}, Daniel P. Stark⁵, Santiago Arribas⁶, William M. Baker^{3,4}, Rachana Bhatawdekar^{7,8}, Rebecca Bowler⁹, Kristan Boyett^{10,11}, Alex J. Cameron¹, Stefano Carniani¹², Stephane Charlot¹³, Jacopo Chevallard¹, Mirko Curti^{14,3,4}, Emma Curtis-Lake¹⁵, Daniel J. Eisenstein¹⁶, Kevin Hainline⁵, Ryan Hausen¹⁷, Zhiyuan Ji⁵, Benjamin D. Johnson¹⁶, Nimisha Kumari¹⁸, Tobias J. Looser^{3,4}, Roberto Maiolino^{3,4,2}, Michael V. Maseda¹⁹, Eleonora Parlanti¹², Hans-Walter Rix²⁰, Brant E. Robertson²¹, Lester Sandles^{3,4}, Jan Scholtz^{3,4}, Renske Smit²², Sandro Tacchella^{3,4}, Hannah Übler^{3,4}, Christina C. Williams²³, and Chris Willott²⁴

(Affiliations can be found after the references)

Received X / Accepted Y

ABSTRACT

The rest-frame UV recombination emission line Ly α can be powered by ionising photons from young massive stars in star forming galaxies, but its ability to be resonantly scattered by neutral gas complicates its interpretation. For reionization era galaxies, a neutral intergalactic medium (IGM) will scatter Ly α from the line of sight, making Ly α a useful probe of the neutral fraction evolution. Here, we explore Ly α in JWST/NIRSpec spectra from the ongoing JADES programme, which targets hundreds of galaxies in the well-studied GOODS-S and GOODS-N fields. These sources are UV-faint ($-20.4 < M_{UV} < -16.4$), and thus represent a poorly-explored class of galaxies. The low spectral resolution ($R \sim 100$) spectra of a subset of 84 galaxies in GOODS-S with $z_{spec} > 5.6$ (as derived with optical lines) are fit with line and continuum models, in order to search for significant line emission. Through exploration of the R100 data, we find evidence for Ly α in 17 sources. This sample allows us to place observational constraints on the fraction of galaxies with Ly α emission in the redshift range $5.6 < z < 7.5$, with a decrease from $z = 6$ to $z = 7$. We also find a positive correlation between Ly α equivalent width and M_{UV} , as seen in other samples. These results are used to estimate the neutral gas fraction at $z \sim 7$, agreeing with previous results ($X_{HI} \sim 0.5 - 0.9$).

Key words. (cosmology:) dark ages, reionization, first stars - (galaxies:) intergalactic medium - galaxies: high-redshift

1. Introduction

By studying the properties of galaxies at high redshift (such as morphology, spectral energy distributions, and kinematics), we are able to chart how populations of galaxies have evolved through cosmic time. In individual galaxies we can study the buildup of gaseous reservoirs, the conversion of this fuel into stars, and the effects of feedback. By studying the overall galaxy population as a function of redshift, we can determine the evolution of the luminosity function, the star formation rate density, and the growth of supermassive black holes. In parallel, these studies shine light on the last great phase transition of the Universe, when the intergalactic medium (IGM) became ionised (i.e., the epoch of reionization; EoR).

This epoch began at the end of the ‘cosmic dark ages’, when the first stars formed (e.g., Villanueva-Domingo et al. 2018). The UV radiation of these objects created ionised regions (i.e., ‘bubbles’), which grew and merged together (e.g., Gnedin 2000). Observations suggest that the IGM was mostly ionised at $z \sim 6$ ($t_H \sim 0.91$ Gyr; e.g., Fan et al. 2006), although the details of reionization are still being derived (e.g., the drivers; Hutchison et al. 2019; Naidu et al. 2020; Endsley et al. 2021, topology; Pentericci et al. 2014; Larson et al. 2022; Yoshioka et al. 2022, and timeline; Christenson et al. 2021; Cain et al. 2021; Zhu et al. 2022). One of the most useful tools for studying this epoch is the bright Lyman- α line of hydrogen ($\lambda = 1215.67\text{\AA}$; hereafter Ly α).

As the lowest-energy transition ($n = 2 \rightarrow 1$) of the most abundant element, Ly α emission should be ubiquitous. But this radiation may be absorbed and re-radiated by any other hydrogen atom in the ground state (i.e., HI). For galaxies at $z \lesssim 6$, this repeated absorption and re-radiation by neutral gas inside a galaxy (i.e., resonant scattering) means that Ly α can be greatly reduced in intensity, but also may be observed along sight lines distant from the original emission region, as seen in large Ly α halos of ~ 10 kpc (e.g., Drake et al. 2022; Kikuta et al. 2023) or ~ 100 kpc (e.g., Steidel et al. 2000; Reuland et al. 2003; Dey et al. 2005; Cai et al. 2017; Li et al. 2021; Guo et al. 2023; Zhang et al. 2023).

For galaxies in the EoR, neutral gas in the IGM surrounding a galaxy may also scatter Ly α emission, resulting in a lower observed brightness (e.g., Fontana et al. 2010; Stark et al. 2010). In order for this emission to be observable, it must lie in an ionised bubble (e.g., Mason & Gronke 2020) and/or feature a significant outflow (e.g., Dijkstra & Wyithe 2010). So by comparing the fraction of galaxies with Ly α emission to the expected number from models (Ly α fraction; $X_{Ly\alpha}$), we are able to place constraints on the HI filling fraction (X_{HI} ; e.g., Ono et al. 2012; Mason et al. 2018; Matthee et al. 2022).

Constraints on $X_{Ly\alpha}$ have been placed for galaxies from $4 \lesssim z \lesssim 8$ (e.g., Stark et al. 2011; Curtis-Lake et al. 2012; Caruana et al. 2012, 2014; Ono et al. 2012; Schenker et al. 2014; Stark et al. 2017; Pentericci et al. 2018; Yoshioka et al. 2022) and down to $z \sim 2$ (e.g., Cassata et al. 2015). By comparing the observed evolution of $X_{Ly\alpha}$ to that expected from different

* E-mail: gareth.jones@physics.ox.ac.uk

$\text{Ly}\alpha$ luminosity functions, some of these works have placed constraints on X_{HI} , suggesting that it quickly decreased from ≥ 0.9 to ~ 0 between $z \sim 8$ and $z \sim 6$ (e.g., Mason et al. 2018, 2019; Morales et al. 2021). Therefore, the study of galaxies in this short time interval (~ 0.3 Gyr) is key to characterising the timeline of reionization. While a number of studies have been undertaken, observations have been hampered by small sample size, limited volume volume (prone to cosmic variance), or a focus on bright ($M_{UV} \lesssim -20$) or strongly lensed sources (e.g., Hoag et al. 2019; Fuller et al. 2020; Bolan et al. 2022). Already, the JWST/Near-Infrared Spectrograph (NIRSpec; Jakobsen et al. 2022; Böker et al. 2023) has seen great success in detecting $\text{Ly}\alpha$ (e.g., Bunker et al. 2023b; Jung et al. 2023; Roy et al. 2023; Tang et al. 2023). But to reduce sample variance and allow stronger conclusions, a wide-area survey down to $M_{UV} \sim -18.75$ is needed (e.g., Taylor & Lidz 2014). With JWST, this survey is now possible.

The JWST Advance Deep Extragalactic Survey (JADES; Bunker et al. 2020; Eisenstein et al. 2023) is a cycle 1-2 GTO programme observing the GOODS (The Great Observatories Origins Deep Survey; Dickinson et al. 2003) north and south fields with JWST/NIRSpec in multi-object spectroscopy mode (Ferruit et al. 2022) in both low spectral resolution (R100) and medium spectral resolution (R1000), in combination with JWST/Near-Infrared Camera (NIRCam; Rieke et al. 2023).

This rich dataset is the subject of numerous ongoing investigations, including detailed modelling of the $\text{Ly}\alpha$ profiles using the R1000 spectra (e.g., asymmetry, velocity offsets; Saxena et al. 2023), analysis of the damping wings (Jakobsen et al. in prep), and a search for $\text{Ly}\alpha$ overdensities that hint at large ionised bubbles (Witstok et al. 2023). In this work, we search for $\text{Ly}\alpha$ emission in the R100 spectra of data from GOODS-S for the purpose of placing constraints on the neutral gas fraction at $z \sim 6 - 8$. These fits are used to examine correlations between $\text{Ly}\alpha$ rest-frame equivalent width ($\text{REW}_{\text{Ly}\alpha}$), redshift, and UV absolute magnitude.

We describe our sample in Section 2. The details and results of our R100 spectral fitting procedure are given in Section 3. These findings are discussed in Section 4, and we conclude in Section 5. We assume a standard concordance cosmology ($\Omega_{\Lambda}, \Omega_m, h$) = (0.7, 0.3, 0.7) throughout.

2. Sample

2.1. Observations overview

JADES consists of two survey depths (i.e., ‘Deep’ and ‘Medium’). The former allows for characterisation of a small number of dimmer galaxies or more detailed study of individual sources at higher S/N, while the latter enables a statistical characterisation of the galaxy population at high- z . In addition, each tier has two stages with different selections: one based on existing Hubble Space Telescope (HST) imaging (followed by ‘HST’) and the other based on JWST/NIRCam imaging (followed by ‘JWST’; see Eisenstein et al. 2023 for more detail).

From the JADES survey, we utilised data from galaxies in GOODS-S in the Deep/HST (PID: 1210, PI: N. Lützgendorf), Medium/HST (PID: 1180, PI: D. Eisenstein), and Medium/JWST (PID: 1286, PI: N. Lützgendorf) subsurveys. Target catalogues were created for each tier, with galaxies assigned priority classes (PCs) based on photometric redshift, apparent UV-brightness, and visual inspection of existing ancillary data (for more details on Deep/HST priority classes, see Bunker et al. 2023a). Galaxies with $z_{\text{phot}} > 5.6$ were collected from studies that selected sources based on the Lyman-break drop out se-

lection (e.g., Bunker et al. 2004; Bouwens et al. 2015; Harikane et al. 2016), or Lyman-break galaxies (LBGs). This system ensures that both rare (e.g., bright, high-redshift, hosts of active galactic nuclei) and representative systems would be observed. Due to the geometrical constraints dictated by mask construction, galaxies were randomly selected for observation from each PC.

Details of the data acquisition and reduction details are given in other works (Curtis-Lake et al. 2023, Carniani et al. in prep), which we summarise here. Targets were observed with three shutters in a three-point nod. In order to improve data quality, sub-pointings were created for each primary pointing by shifting the JWST/NIRSpec Multi-Shutter Array (MSA) by a few shutters in each direction. Due to failed shutters, not all targets were observable in all three sub-pointings. This results in exposure times of sources in R100 for Deep/HST of 33.6-100.8 ks for 253 observed sources. Medium/JWST features a similar setup, but with a lower R100 exposure time per target: 5.3-8.0 ks for 169 observed sources. While 1354 galaxies were observed in Medium/HST, the majority of the executions (8/12) were negatively affected by a short circuit in the MSA, making the data unusable. The mean exposure time for R100 per object of the usable data is 3.8 ks (Eisenstein et al. 2023). Observations were repeated for some of these objects with unusable data (364 sources), with a mean R100 exposure time per object of 7.5 – 11.3 ks.

The resulting raw data were calibrated using a pipeline developed by the ESA NIRSpec Science Operations Team (SOT) and the NIRSpec GTO Team, which includes corrections for outlier rejection (e.g., ‘snowballs’), background subtraction (using adjacent slits), wavelength grid resampling, and slit loss. This results in 2D spectra with data quality flags, which was used to extract a 1D spectrum and a noise spectrum.

2.2. Sample construction

The resulting spectra of all observed sources were visually inspected and strong emission lines (e.g., [OIII] λ 5007, H α) were fit. We impose a lower redshift limit of $z_{\text{spec}} > 5.6$ in order to ensure a sample of LBGs. This yields a sample of 84 galaxies at $z \gtrsim 5.6$ (38 from Medium/HST, 13 from Medium/JWST, and 33 from Deep/HST) with precise spectroscopic redshifts (full details in Bunker et al. 2023a). Both R100 and R1000 spectra are available for these galaxies, and we proceed with the R100 spectra in this work¹.

Our sample of 84 galaxies is composed of galaxies at $z_{\text{spec}} > 5.6$ (i.e., LBGs) with cuts on UV brightness in HST broadband filters redward of the Lyman break. Some sources were excluded from our sample for a lack of strong emission lines (i.e., a poorly constrained z_{spec}). While this results in a more complex sample than the uniform sample selection of some previous studies (e.g., Pentericci et al. 2018; Yoshioka et al. 2022), this inhomogeneity is taken into account through the error spectrum of each source and a completeness analysis.

3. Combined $\text{Ly}\alpha$ and continuum fit

At these high redshifts, the spectra exhibit a strong continuum break at the $\text{Ly}\alpha$ wavelength at the redshift of the galaxy. The deep sensitivity of the R100 data allows us to simultaneously characterise any $\text{Ly}\alpha$ emission and the underlying continuum of

¹ Details of the R1000 analysis are presented in an associated paper (Saxena et al. 2023)

each source. To do this, we examine whether a two-component model (i.e., line and continuum) or a single-component model (i.e., only continuum) better fits the extracted spectrum of each source using `LMFIT` (Newville et al. 2014). This process is detailed below.

3.1. Resolution effects

Due to the low spectral resolution of the R100 data, we must consider both the wavelength grid and spectral dispersion. The spectral pixels in our calibrated data are large ($\Delta v \sim 2000 - 2600 \text{ km s}^{-1}$ per pixel at the redshifted Ly α wavelength for galaxies at $z \sim 5.6 - 10$). Furthermore, for galaxies observed in the EoR this wavelength is near the minimum of the PRISM resolving power curve², with $R \sim 30$. This implies that the line-spread function (LSF) has a full width at half maximum (FWHM) of $\sim 10^4 \text{ km s}^{-1}$. Although for a compact source which does not fill the slit, the resolving power will in practice be higher by as much as a factor of 2 (De Graaff et al. in prep).

The low resolution also makes it impossible to characterise the Ly α profile (e.g., asymmetry, velocity offset). Instead, the Ly α emission may be approximated as additional flux in the first spectral bin redward of the Ly α break, which is spread into neighbouring bins by the LSF.

To demonstrate how this affects the interpretation of R100 spectra, we first create a higher-resolution ($\Delta\lambda = 0.001 \mu\text{m}$, or $R \sim 730$) model of a Ly α break (modelled as a step function) at $z = 7$ with no Ly α flux (blue line in the top panel of Figure 1). If we account for the LSF by convolving the spectrum with a Gaussian ($\sigma_R = \lambda_{\text{Ly}\alpha}/R/2.355$), the break becomes an S-shaped curve instead (orange histogram). Rebinning this curve to the coarser R100 wavelength grid maintains the curve, but at lower resolution (green histogram).

If we add Ly α flux with a given $\text{REW}_{\text{Ly}\alpha}$ to the intrinsic high-resolution model as additional flux in the first spectral bin redward of the Ly α break, convolve the model with the LSF, and rebin the result to the R100 spectral grid, we find the profiles shown in the lower panel of Figure 1. The line flux is spread from one low-resolution pixel into a Gaussian that spans both sides of the Ly α break. Even high- $\text{REW}_{\text{Ly}\alpha}$ lines (e.g., 100 \AA) have low peaks (here $4\times$ the continuum level). In addition, low- $\text{REW}_{\text{Ly}\alpha}$ lines ($< 20 \text{ \AA}$) feature very low amplitudes, and instead appear similar to a pure continuum model with a blueshifted Ly α break.

With this in mind, our model fitting procedure begins with a high-resolution spectral model, which is convolved with a Gaussian to account for the resolving power and then rebinned to the R100 spectral grid. This allows us to compare the observed and model spectra directly, in order to extract the intrinsic continuum and Ly α flux.

3.2. Model description

We first assume that the underlying continuum can be approximated by a power law and use a Heaviside step function to represent the Ly α break (see Appendix A for a discussion of this assumption). This continuum-only model only features two variables: the continuum value at a rest-frame wavelength of 1500 \AA ($S_{C,o}$) and the spectral slope just redwards of Ly α (n ; $\sim 1300 - 1500 \text{ \AA}$ rest-frame), which is not fixed to the redder

² As recorded in the JWST documentation; <https://jwst-docs.stsci.edu/jwst-near-infrared-spectrograph/nirspec-instrumentation/nirspec-dispersers-and-filters>

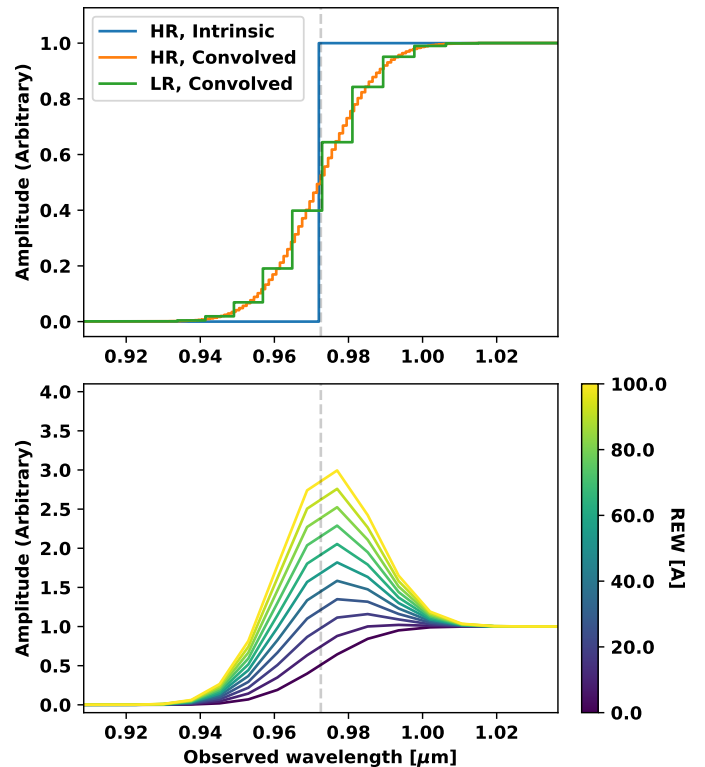


Fig. 1. Demonstration of how Ly α break and emission for a source at $z = 7$ are affected by the low resolving power of our observations. The top panel shows how a step function (blue line) is affected by the resolving power on a high-resolution ($\Delta\lambda = 0.001 \mu\text{m}$) spectral grid (orange curve), and how this curve would appear on the R100 spectral grid (green steps). If we add Ly α emission with a given $\text{REW}_{\text{Ly}\alpha}$ in the first high-resolution spectral bin redwards of the break and then account for the LSF and R100 spectral bin, we find the curves in the lower panel.

(i.e., $\sim 1400 - 2300 \text{ \AA}$ rest-frame) spectral slope β derived by Saxena et al. (2023).

In the case where both continuum and Ly α emission are detected, the line emission will have a rest-frame equivalent width:

$$\text{REW}_{\text{Ly}\alpha} = \frac{F_{\text{Ly}\alpha}}{(1+z)S_C(\lambda_{\text{Ly}\alpha, \text{obs}})} \quad (1)$$

where $F_{\text{Ly}\alpha}$ is the total line flux of Ly α . As discussed in Section 3.1, the low spectral resolution of the R100 data dictates that our line emission model is simple. Our combined line and continuum model thus has three variables: those of the continuum model (i.e., $S_{C,o}$ and n) and $\text{REW}_{\text{Ly}\alpha}$.

For both the continuum and line+continuum models, we first create a spectral grid of high resolution ($\Delta\lambda = 0.001 \mu\text{m}$) and populate each bin using a continuum-only or continuum and line model. As discussed in Section 3.1, we then convolve the spectrum with a Gaussian that accounts for the LSF. We first consider using a Gaussian based on the theoretical resolving power as recorded in the JWST documentation ($\sigma_R = \lambda_{\text{Ly}\alpha}/R/2.355$). However, this was calculated assuming a source that illuminates the slit uniformly, which is not the case for the relatively compact sources in our sample. Detailed LSFs for the sources in Deep/HST have been calculated (de Graaff et al. in prep), which reveal that the actual LSF is smaller than the theoretical value, by a factor of up to ~ 2.4 . However these models are not available for our whole sample. To account for the LSF in a uniform manner, we convolve the model spectrum with a Gaussian of width

$F_R\sigma_R$, where F_R is allowed to vary. These data are then rebinned to the R100 spectral grid of an observation.

3.3. Fitting procedure

We use `LMFIT` with a ‘leastsq’ minimiser to fit each convolved model to a subset of the observed spectrum. Each data point is weighted by its associated inverse variance (as derived from the error spectrum).

We limit the fit subset to the wavelength range $[(\lambda_{Ly\alpha} \pm (0.03\mu\text{m})) \times (1+z)]$, with a minimum of $\geq 0.75\mu\text{m}$. This range is chosen to avoid including excessive amounts of noisy data at blue wavelengths below the $Ly\alpha$ break, and to only fit the continuum just redwards of $Ly\alpha$, avoiding nearby emission lines (e.g., [CIV] $\lambda\lambda$ 1548, 1551, HeII λ 1640).

While precise systemic redshifts for each source have been derived using fits to strong lines (e.g., [OIII] λ 5007, H α) using the higher spectral resolution gratings (Bunker et al. 2023a), it is possible that the $Ly\alpha$ emission is shifted into a neighbouring spectral bin by a large velocity offset (i.e., up to a few hundred km s^{-1} ; Erb et al. 2014; Marchi et al. 2019) or a different binning scheme between the gratings and prism. This is accounted for by allowing the redshift of $Ly\alpha$ emission to vary from the systemic redshift within the R100 bin, taking the result with the lowest χ^2 .

Next, we consider the lowest REW line that we can detect for each source. Because the line emission is spread from one into multiple channels by convolution with the LSF, we may approximate the 1σ limit on $REW_{Ly\alpha}$ in the R100 spectrum as:

$$\Delta REW_{Ly\alpha,1\sigma} = \frac{\sqrt{2\pi}E(\lambda_{Ly\alpha,obs})F_R\sigma_R}{(1+z)S_{C,Ly\alpha}} \quad (2)$$

where $F_R\sigma_R$ is the width of the LSF and $E(\lambda)$ is the error spectrum.

The results of the continuum (‘C’) and line and continuum (‘L+C’) are examined, and a definite $Ly\alpha$ detection is reported if both of the following criteria are met:

- The ‘L+C’ fit features a lower χ_{red}^2 than the ‘C’ fit.
- The best-fit $REW_{Ly\alpha}$ is greater than $2.5\Delta REW_{Ly\alpha,1\sigma}$.

When $Ly\alpha$ is detected, we take the best-fit $REW_{Ly\alpha}$ value and its associated uncertainty from our fit. Otherwise, we treat the $Ly\alpha$ line as undetected, and use $3\Delta REW_{Ly\alpha,1\sigma}$ as an upper limit.

3.4. Results

With this definition, we find that 17 galaxies in our sample feature significant $Ly\alpha$ emission from the R100 spectra alone. The best-fit models of these detections are shown in Figures 2, 3, and 4, while the best-fit parameters of all galaxies in our sample are presented in Table 1.

For comparison, we present $REW_{Ly\alpha}$ values derived by taking the continuum values from this work and the $Ly\alpha$ fluxes measured from the R1000 spectra by Saxena et al. (2023). These line fluxes were only measured for galaxies at $z > 5.8$ in the Deep/HST and Medium/HST tiers in GOODS-S (excluding Medium/JWST, where there are no $z > 5.8$ galaxies detected in $Ly\alpha$ emission). For some of these sources, $Ly\alpha$ fell into the unobservable chip gap, so no $Ly\alpha$ is given.

We note that the use of the low spectral resolution PRISM/CLEAR grating/filter combination ($R \sim 100$) results in detections or limits that are in agreement (i.e., within 3σ) with

the higher-resolution R1000 data for every source. This is encouraging, as the latter is more sensitive to low equivalent width lines. For example, Bunker et al. (2023b) find that $Ly\alpha$ is not observable in the R100 spectrum of GNz-11, but is clearly detected in the R1000 spectrum. This can also be seen in our sources that are undetected in the prism, but have a 3σ $REW_{Ly\alpha,R100}$ upper limit that agrees with a smaller $REW_{Ly\alpha,R1000}$ value (i.e. our $REW_{Ly\alpha}$ upper limit from the prism is consistent with the value of the $REW_{Ly\alpha}$ inferred from the grating detection).

From our R100 fitting analysis, we find that 17 of the 84 galaxies in our sample are detected in $Ly\alpha$. In the following subsections, we analyze the properties of these detections.

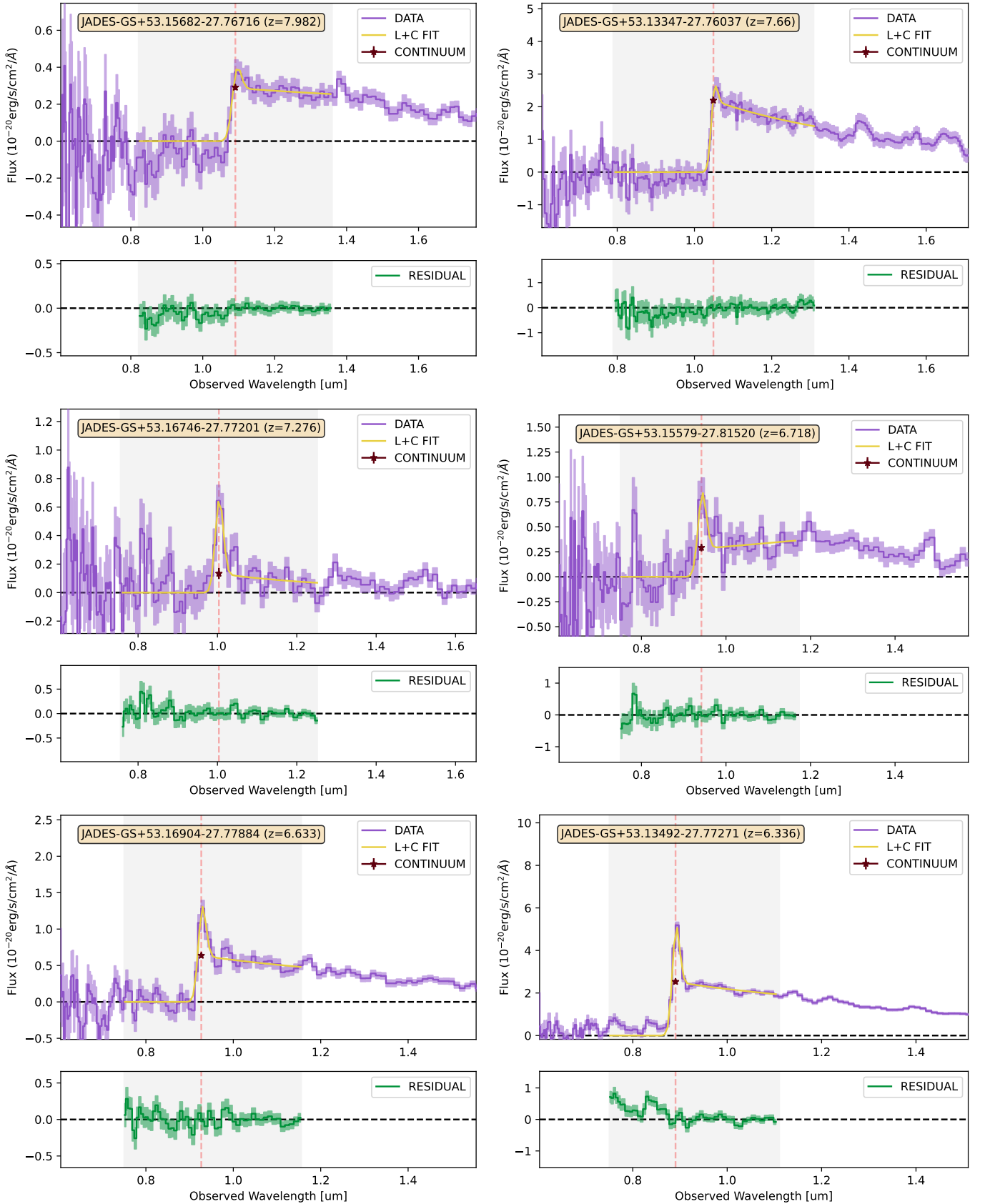


Fig. 2. Results of fitting a line + continuum model to observed JADES R100 data, for sources detected in Ly α emission (denoted by ‘L+C FIT’). In each top panel, we show the observed spectrum (purple line) with an associated 1σ error (shaded region). The best-fit model, which includes the effects of the LSF, is shown by a yellow line. Fitting was performed using the wavelength range that is shaded grey. The continuum value at the redshifted Ly α wavelength is represented by a brown star. The bottom panel shows the residual.

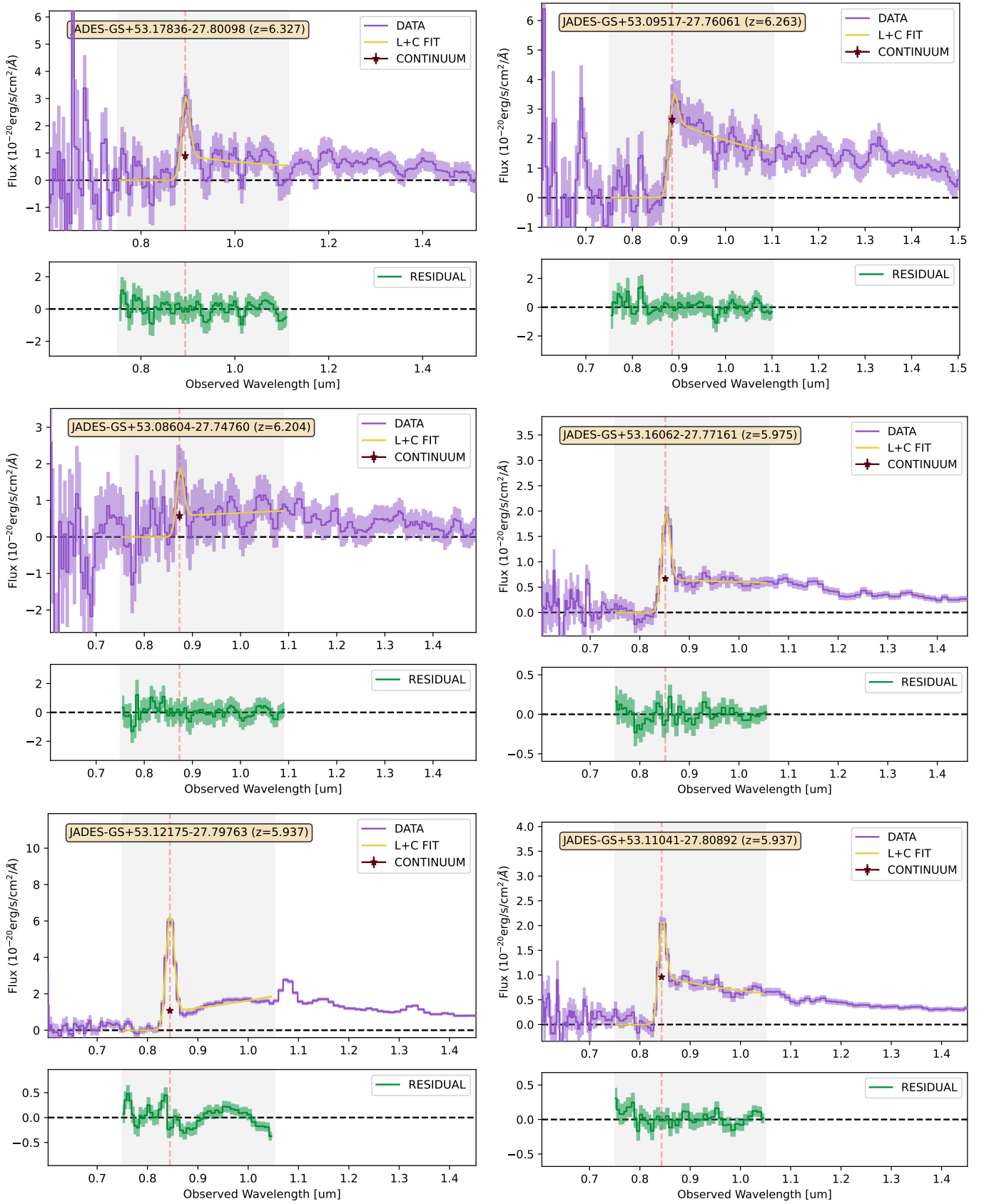


Fig. 3. See caption of Figure 2.

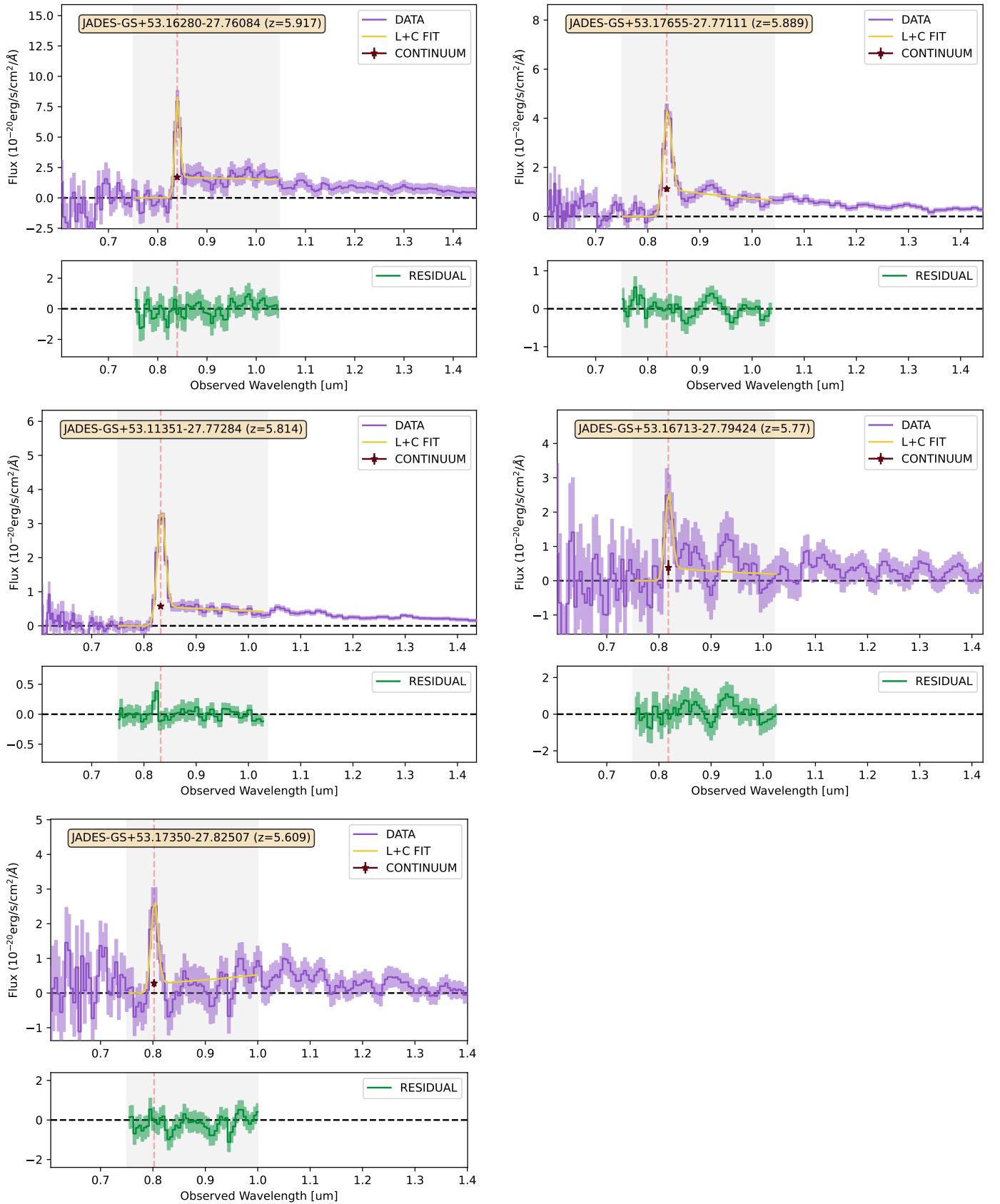


Fig. 4. See caption of Figure 2.

Table 1. Results of fitting R100 spectra of each galaxy. We include the best-fit M_{UV} (from the spectrum, see Appendix D) and continuum flux at the redshifted Ly α wavelength. Line fluxes and rest-frame equivalent widths from the R100 data alone are shown first. Next, REW values derived by combining the R1000-based Ly α fluxes from Saxena et al. (2023) with our R100 continuum values are presented for reference. Systemic redshifts (based on fits to strong optical lines) have uncertainty of 0.001 (Bunker et al. 2023a). Upper limits are given as 3σ . Galaxies detected in Ly α emission in the R100 data are listed first.

ID	z_{sys}	Tier	M_{UV}	$S_C(\lambda_{Ly\alpha,obs})$ $10^{-21} \text{ erg s}^{-1} \text{ cm}^{-2} \text{ \AA}^{-1}$	$F_{Ly\alpha,R100}$ $10^{-19} \text{ erg s}^{-1} \text{ cm}^{-2}$	$REW_{Ly\alpha,R100}$ \AA	$F_{Ly\alpha,R100}$ $10^{-19} \text{ erg s}^{-1} \text{ cm}^{-2}$	$REW_{Ly\alpha,R100}$ \AA
<i>JADES-GS</i>								
+53.15682-27.76716	7.982	Deep/HST	-18.71 ± 0.05	2.9 ± 0.1	7 ± 1	27 ± 5	7 ± 1	27 ± 8
+53.13347-27.76037	7.660	Medium/HST	-20.43 ± 0.03	21.9 ± 0.6	25 ± 4	13 ± 2	42 ± 3	22 ± 3
+53.16746-27.7201	7.276	Deep/HST	-17.00 ± 0.25	1.3 ± 0.4	15 ± 7	134 ± 50	23 ± 2	207 ± 27
+53.15579-27.81520	6.718	Deep/HST	-18.51 ± 0.08	2.9 ± 0.4	17 ± 5	77 ± 22	27 ± 3	122 ± 27
+53.16904-27.77884	6.633	Deep/HST	-18.76 ± 0.04	6.4 ± 0.3	21 ± 3	44 ± 6	22 ± 5	45 ± 20
+53.13492-27.77271	6.336	Deep/HST	-20.11 ± 0.01	25.3 ± 0.8	72 ± 6	39 ± 3	77 ± 4	41 ± 4
+53.17836-27.80098	6.327	Medium/HST	-18.75 ± 0.18	9.0 ± 1.8	57 ± 20	86 ± 26	43 ± 12	65 ± 36
+53.09517-27.76061	6.263	Medium/HST	-19.85 ± 0.06	26.4 ± 1.7	42 ± 9	22 ± 5	31 ± 8	16 ± 8
+53.08604-27.74760	6.204	Medium/HST	-18.93 ± 0.14	5.8 ± 1.3	29 ± 13	70 ± 27	48 ± 21	114 ± 99
+53.16062-27.77161	5.975	Deep/HST	-18.63 ± 0.04	6.7 ± 0.3	33 ± 3	72 ± 6	22 ± 5	47 ± 20
+53.12175-27.79763	5.937	Deep/HST	-19.83 ± 0.01	10.7 ± 0.7	123 ± 13	165 ± 15	106 ± 9	142 ± 25
+53.11041-27.80892	5.937	Deep/HST	-18.68 ± 0.03	9.6 ± 0.5	29 ± 3	44 ± 5	29 ± 6	43 ± 19
+53.16280-27.76084	5.917	Medium/HST	-19.60 ± 0.08	17.1 ± 1.8	90 ± 17	76 ± 12	112 ± 19	95 ± 32
+53.17655-27.77111	5.889	Deep/HST	-18.72 ± 0.06	11.2 ± 1.1	74 ± 12	95 ± 12	—	—
+53.11351-27.77284	5.814	Deep/HST	-18.18 ± 0.05	5.7 ± 0.5	60 ± 8	153 ± 17	—	—
+53.16713-27.79424	5.770	Medium/HST	-17.32 ± 0.60	3.8 ± 2.2	41 ± 36	159 ± 106	—	—
+53.17350-27.82507	5.609	Medium/JWST	-18.23 ± 0.19	2.8 ± 1.2	44 ± 29	238 ± 120	—	—
+53.16477-27.77463	11.900	Deep/HST	-19.36 ± 0.05	1.6 ± 0.2	< 5	< 23	—	—
+53.15884-27.77349	9.870	Deep/HST	-18.45 ± 0.11	1.1 ± 0.2	< 7	< 58	—	—
+53.16735-27.80750	9.690	Deep/HST	-19.27 ± 0.04	3.1 ± 0.1	< 5	< 14	—	—
+53.11243-27.77461	9.440	Deep/HST	-20.36 ± 0.01	8.8 ± 0.2	< 5	< 5	—	—
+53.16446-27.80218	8.482	Deep/HST	-17.54 ± 0.20	0.5 ± 0.1	< 8	< 161	—	—
+53.08722-27.77706	7.580	Medium/HST	-19.03 ± 0.20	6.8 ± 1.1	< 56	< 95	—	—
+53.18343-27.79097	7.429	Medium/JWST	-20.00 ± 0.05	11.3 ± 0.7	< 37	< 39	—	—
+53.19105-27.79731	7.266	Medium/JWST	-19.15 ± 0.10	6.0 ± 0.5	< 30	< 60	—	—
+53.18714-27.80129	7.264	Medium/JWST	-18.41 ± 0.20	3.5 ± 0.6	< 35	< 122	—	—
+53.15283-27.80194	7.262	Deep/HST	-17.95 ± 0.10	2.0 ± 0.3	< 8	< 48	—	—
+53.18374-27.79390	7.262	Medium/JWST	-17.94 ± 0.36	2.9 ± 0.8	< 40	< 170	—	—
+53.16483-27.78826	7.250	Medium/HST	-19.08 ± 0.18	8.9 ± 1.2	< 58	< 79	—	—
+53.16172-27.78539	7.240	Medium/HST	-19.47 ± 0.18	7.7 ± 1.0	< 65	< 103	—	—
+53.16556-27.77266	7.240	Medium/HST	-18.32 ± 0.29	4.6 ± 1.8	< 45	< 119	—	—
+53.11833-27.76901	7.206	Deep/HST	-18.80 ± 0.05	5.1 ± 0.3	< 10	< 25	—	—
+53.13806-27.78186	7.140	Medium/HST	-18.66 ± 0.22	1.8 ± 0.4	< 46	< 312	—	—
+53.13423-27.76891	7.052	Deep/HST	-18.84 ± 0.06	7.6 ± 0.5	< 12	< 19	—	—
+53.17688-27.78156	7.002	Medium/JWST	-17.94 ± 0.28	1.2 ± 0.5	< 31	< 334	—	—
+53.18302-27.78946	6.951	Medium/JWST	-17.92 ± 0.27	1.4 ± 0.5	< 30	< 271	—	—
+53.11730-27.76408	6.930	Deep/HST	-18.69 ± 0.07	4.7 ± 0.3	< 13	< 35	—	—
+53.14771-27.71537	6.846	Medium/HST	-20.33 ± 0.05	22.3 ± 1.3	< 45	< 26	—	—
+53.11817-27.79302	6.800	Medium/HST	-19.01 ± 0.13	7.2 ± 1.1	< 41	< 74	—	—
+53.11634-27.76194	6.794	Medium/HST	-18.88 ± 0.12	7.3 ± 1.1	< 34	< 61	—	—
+53.15138-27.81917	6.711	Deep/HST	-17.96 ± 0.07	3.8 ± 0.3	< 7	< 25	—	—

Table 1. Results of fitting R100 spectra of each galaxy. We include the best-fit M_{UV} (from the spectrum, see Appendix D) and continuum flux at the redshifted Ly α wavelength. Line fluxes and rest-frame equivalent widths from the R100 data alone are shown first. Next, REW values derived by combining the R1000-based Ly α fluxes from Saxena et al. (2023) with our R100 continuum values are presented for reference. Systemic redshifts (based on fits to strong optical lines) have uncertainty of 0.001 (Bunker et al. 2023a). Upper limits are given as 3σ . Galaxies detected in Ly α emission in the R100 data are listed first.

ID	z_{sys}	Tier	M_{UV}	$S_C(\lambda_{Ly\alpha,obs})$ $10^{-21} \text{ erg s}^{-1} \text{ cm}^{-2} \text{ \AA}^{-1}$	$F_{Ly\alpha,R100}$ $10^{-19} \text{ erg s}^{-1} \text{ cm}^{-2}$	$REW_{Ly\alpha,R100}$ \AA	$F_{Ly\alpha,R100}$ $10^{-19} \text{ erg s}^{-1} \text{ cm}^{-2}$	$REW_{Ly\alpha,R100}$ \AA
<i>JADES-GS</i>								
+53.10538-27.72347	6.636	Medium/HST	-20.48 ± 0.04	27.0 ± 1.4	< 63	< 31	—	—
+53.15160-27.78791	6.629	Medium/JWST	-17.02 ± 0.34	1.2 ± 0.5	< 20	< 208	—	—
+53.16288-27.76928	6.624	Deep/HST	-17.61 ± 0.20	2.0 ± 0.5	< 16	< 107	—	—
+53.13743-27.76519	6.622	Medium/HST	-18.43 ± 0.26	6.8 ± 2.0	< 51	< 97	25 ± 10	48 ± 40
+53.16951-27.75331	6.620	Medium/HST	-19.34 ± 0.11	12.9 ± 1.6	< 46	< 47	—	—
+53.12731-27.78805	6.390	Medium/HST	-19.43 ± 0.13	18.4 ± 2.1	< 62	< 46	—	—
+53.12556-27.78676	6.390	Medium/HST	-18.36 ± 0.34	5.7 ± 2.0	< 59	< 139	—	—
+53.19660-27.81345	6.340	Medium/HST	-18.24 ± 0.28	5.4 ± 1.0	< 42	< 105	—	—
+53.17582-27.77446	6.336	Deep/HST	-18.74 ± 0.06	6.4 ± 0.6	< 15	< 32	—	—
+53.16660-27.77240	6.330	Deep/HST	-18.56 ± 0.05	6.7 ± 0.4	< 9	< 18	—	—
+53.15516-27.76072	6.314	Medium/HST	-19.42 ± 0.05	15.9 ± 0.8	< 27	< 23	—	—
+53.16613-27.77204	6.300	Medium/HST	-18.47 ± 0.25	7.3 ± 1.9	< 52	< 98	—	—
+53.16238-27.80332	6.298	Deep/HST	-16.33 ± 0.62	1.0 ± 0.6	< 15	< 195	—	—
+53.08311-27.78635	6.260	Medium/HST	-19.72 ± 0.09	17.8 ± 2.2	< 62	< 48	—	—
+53.16902-27.80079	6.250	Medium/HST	-18.95 ± 0.16	10.9 ± 1.5	< 48	< 61	—	—
+53.20800-27.79005	6.180	Medium/HST	-19.25 ± 0.16	5.2 ± 1.8	< 90	< 242	—	—
+53.15613-27.77584	6.107	Deep/HST	-19.02 ± 0.04	8.4 ± 0.6	< 11	< 19	—	—
+53.15953-27.77152	6.100	Medium/HST	-20.43 ± 0.04	40.7 ± 1.7	< 43	< 15	—	—
+53.19588-27.76843	6.060	Medium/HST	-18.80 ± 0.16	7.7 ± 1.6	< 41	< 75	—	—
+53.17324-27.79567	6.000	Medium/HST	-19.66 ± 0.06	15.3 ± 1.1	< 33	< 31	—	—
+53.17264-27.76706	5.990	Medium/HST	-19.02 ± 0.12	9.5 ± 1.4	< 42	< 63	—	—
+53.19938-27.79627	5.980	Medium/HST	-19.44 ± 0.09	17.2 ± 1.4	< 42	< 35	—	—
+53.14902-27.78070	5.956	Medium/JWST	-17.85 ± 0.34	4.4 ± 1.6	< 37	< 121	—	—
+53.11911-27.76080	5.949	Deep/HST	-19.42 ± 0.02	17.7 ± 0.5	< 7	< 6	—	—
+53.11264-27.77262	5.934	Medium/HST	-18.41 ± 0.22	4.9 ± 1.7	< 41	< 120	—	—
+53.12654-27.81809	5.932	Deep/HST	-18.93 ± 0.04	10.7 ± 0.6	< 10	< 13	—	—
+53.13044-27.80236	5.930	Medium/HST	-19.17 ± 0.11	7.8 ± 1.8	< 71	< 131	—	—
+53.15218-27.77840	5.927	Medium/JWST	-16.99 ± 0.43	0.9 ± 0.5	< 19	< 316	—	—
+53.10547-27.76115	5.925	Medium/HST	-20.09 ± 0.05	18.0 ± 1.4	< 42	< 33	—	—
+53.12259-27.76057	5.920	Deep/HST	-19.64 ± 0.02	24.0 ± 0.6	< 9	< 6	—	—
+53.14987-27.75283	5.919	Medium/HST	-19.39 ± 0.07	13.7 ± 1.0	< 33	< 35	—	—
+53.17752-27.80252	5.860	Medium/HST	-19.15 ± 0.11	15.2 ± 1.3	< 40	< 38	—	—
+53.14197-27.75523	5.827	Medium/HST	-19.70 ± 0.08	24.8 ± 1.6	< 41	< 24	—	—
+53.16730-27.80287	5.818	Deep/HST	-17.89 ± 0.09	3.2 ± 0.3	< 9	< 43	—	—
+53.15407-27.76607	5.807	Deep/HST	-18.94 ± 0.04	10.3 ± 0.6	< 9	< 13	—	—
+53.12554-27.75505	5.780	Medium/HST	-19.35 ± 0.11	9.3 ± 1.7	< 57	< 90	—	—
+53.13385-27.77858	5.778	Medium/JWST	-16.72 ± 0.73	2.1 ± 1.3	< 28	< 200	—	—
+53.14505-27.81643	5.774	Deep/HST	-18.05 ± 0.10	4.7 ± 0.7	< 13	< 40	—	—
+53.11537-27.81477	5.770	Deep/HST	-19.32 ± 0.03	14.4 ± 0.7	< 12	< 13	—	—
+53.11775-27.81653	5.761	Medium/JWST	-17.84 ± 0.32	6.2 ± 1.7	< 36	< 85	—	—
+53.21160-27.79639	5.760	Medium/HST	-19.35 ± 0.10	7.3 ± 1.1	< 43	< 88	—	—

Table 1. Results of fitting R100 spectra of each galaxy. We include the best-fit M_{UV} (from the spectrum, see Appendix D) and continuum flux at the redshifted Ly α wavelength. Line fluxes and rest-frame equivalent widths from the R100 data alone are shown first. Next, REW values derived by combining the R1000-based Ly α fluxes from Saxena et al. (2023) with our R100 continuum values are presented for reference. Systemic redshifts (based on fits to strong optical lines) have uncertainty of 0.001 (Bunker et al. 2023a). Upper limits are given as 3σ . Galaxies detected in Ly α emission in the R100 data are listed first.

ID	z_{sys}	Tier	M_{UV}	$S_C(\lambda_{\text{Ly}\alpha, \text{obs}})$ $10^{-21} \text{ erg s}^{-1} \text{ cm}^{-2} \text{ \AA}^{-1}$	$F_{\text{Ly}\alpha, \text{R100}}$ $10^{-19} \text{ erg s}^{-1} \text{ cm}^{-2}$	$\text{REW}_{\text{Ly}\alpha, \text{R100}}$ \AA	$F_{\text{Ly}\alpha, \text{R100}}$ $10^{-19} \text{ erg s}^{-1} \text{ cm}^{-2}$	$\text{REW}_{\text{Ly}\alpha, \text{R100}}$ \AA
<i>JADES-GS</i>								
+53.13059-27.80771	5.617	Deep/HST	-18.58 ± 0.09	9.9 ± 1.3	< 18	< 27	–	–
+53.18064-27.82239	5.606	Medium/JWST	-20.12 ± 0.03	29.3 ± 1.4	< 29	< 15	–	–

3.5. Completeness analysis

As seen in equation 2, our REW sensitivity is dependent on observational parameters (error spectrum and LSF) as well as source properties (redshift and continuum flux). To further complicate matters, the error spectrum features higher values at small wavelengths, resulting in larger uncertainties in $E(\lambda_{Ly\alpha,obs})$ for lower redshift sources. Our sample is quite diverse in redshift, continuum strength (i.e., M_{UV}), and sensitivity (i.e., Deep and Medium tiers). So while equation 2 may be used as a limit on REW, it does not capture the breadth of galaxy properties in our sample, and an estimation of the completeness of our sample is required (e.g., Thai et al. 2023).

To begin, we assume a similar model to the previous subsections: a power-law continuum, a Ly α break given by a Heaviside step function, and Ly α emission quantified as an REW. The mean uncertainty spectra for each tier are calculated by averaging the corresponding error spectra. For each galaxy, we take the best-fit continuum strength (M_{UV}) and redshift (z), and create 50 mock spectra by sampling from uniform distributions of $\beta = [-2.5, 2.5]$, and $F_R = [0.1, 0.8]$. This process is repeated for three REW values (25Å, 50Å, 75Å). Gaussian noise is added based on the error spectrum. Each of these 12900 model spectra is fit with the procedure outlined in Section 3.3, and the completeness for each galaxy and REW value is then estimated as the fraction of models that are well fit (i.e., that return a REW value within 3σ of the input value).

This analysis yields an average completeness for our sample of $C_{25\text{Å}} = 0.33$, $C_{50\text{Å}} = 0.60$, and $C_{75\text{Å}} = 0.74$. As expected, the completeness of each tier increases with REW. Our completeness at REW = 25Å is low, which results in poor constraints on $X_{Ly\alpha}$ and X_{HI} (see Section 4.3 and 4.4). We will use these completeness values to derive corrected Ly α fractions in the next Section.

4. Discussion

4.1. Source properties

To demonstrate the multi-tier complexity of our sample, we show the systemic redshift (based on the identification of rest-frame optical lines; Bunker et al. 2023a) and the 1500Å continuum magnitude (hereafter M_{UV}), separated by survey tier (Figure 5). Previous studies defined UV-faint galaxies as those with $M_{UV} > -20.25$ (e.g., Curtis-Lake et al. 2012), which shows that most of the JADES sample contains faint sources. The high-redshift bins ($z > 8$) are dominated by the Deep/HST sources, but the $5.6 < z < 7.5$ regime is well explored by all three subsamples. The overall sample is well sampled in the $M_{UV} \sim -19.5$ to -17.5 regime, but extends down to $M_{UV} \sim -16.5$.

The sources with Ly α detections in R100 data are contained within $z \sim 5.6 - 8.0$, and span a wide range of $M_{UV} \sim -20.5$ to -17 . Of the 51 sources in the Medium tiers, 7 are detected in Ly α ($\sim 14\%$). On the other hand, 10 of the 33 Deep galaxies are Ly α -detected ($\sim 30\%$). In the next subsection, we will explore the limits that the non-detections imply.

4.2. Equivalent width - UV magnitude relation

A recent analysis of JWST/NIRSpec MSA data (CEERS; Tang et al. 2023) and data at lower redshift showed a positive correlation between REW $_{Ly\alpha}$ and M_{UV} for a sample of galaxies with high O32 values (i.e., a high level of ionisation). To investigate this relation further, we first collect a literature sample of

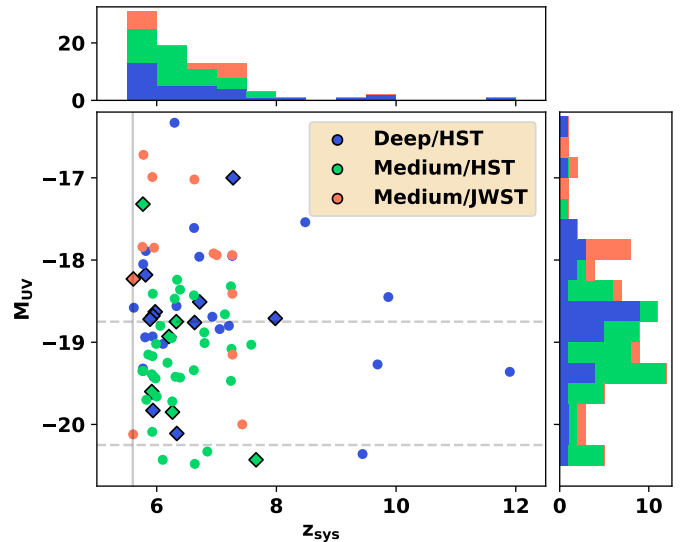


Fig. 5. M_{UV} (from NIRSpec spectra, see Appendix B) versus systemic redshift (based on optical lines) for our sample. Galaxies observed in different tiers are coloured differently. Sources detected in Ly α emission are shown as diamonds with black outlines. Vertical dashed lines show M_{UV} values of -18.75 and -20.25 , while the vertical grey line shows our lower redshift cutoff ($z_{sys} > 5.6$)

galaxies with reported spatial positions, spectroscopic redshifts, REW $_{Ly\alpha}$ from spectral observations, and M_{UV} values (including that of Tang et al. 2023; see Appendix C) and split this sample into different redshift bins (Figure 6).

In each redshift bin, there appears to be a positive correlation between REW $_{Ly\alpha}$ and M_{UV} , such that UV-fainter (higher M_{UV}) objects feature higher Ly α equivalent widths. To illustrate this, we fit a simple model to the data, resulting in positive slopes (see black dashed line). We do not present the fit values or uncertainty, as the literature sample is not constructed with a single set of criteria.

While this trend may be physical, it may also be influenced by the sensitivity limits of observations. As a test of this, we create a set of simulated R100 spectra that do not feature any relation between REW and M_{UV} , fit them with our method, and plot the resulting best-fit values and upper limits (see Appendix D). This test shows that we are not able to recover UV-faint, low-REW galaxies, resulting in an apparent positive correlation. While this does not affect the conclusion of other works, we may not claim a correlation based on our data.

4.3. Ly α fraction

Next, we derive the fraction of galaxies in our sample that are detected in Ly α emission ($X_{Ly\alpha}$). This has been a focus of multiple studies over the past decade (e.g., Stark et al. 2011; Curtis-Lake et al. 2012; Ono et al. 2012; Caruana et al. 2012, 2014; Schenker et al. 2014; Stark et al. 2017; Pentericci et al. 2018; Yoshioka et al. 2022), where subsamples are usually created according to cuts on M_{UV} and the value of REW $_{Ly\alpha}$.

The most well-studied sample for $X_{Ly\alpha}$ evolution is that of galaxies with $-21.75 < M_{UV} < -20.25$ and REW $_{Ly\alpha} > 25\text{Å}$ (e.g., Fontana et al. 2010; Stark et al. 2011; Ono et al. 2012; Curtis-Lake et al. 2012; Schenker et al. 2012, 2014; Pentericci et al. 2014; Cassata et al. 2015; Stark et al. 2017; Pentericci et al. 2018; Yoshioka et al. 2022). For these galaxies, studies

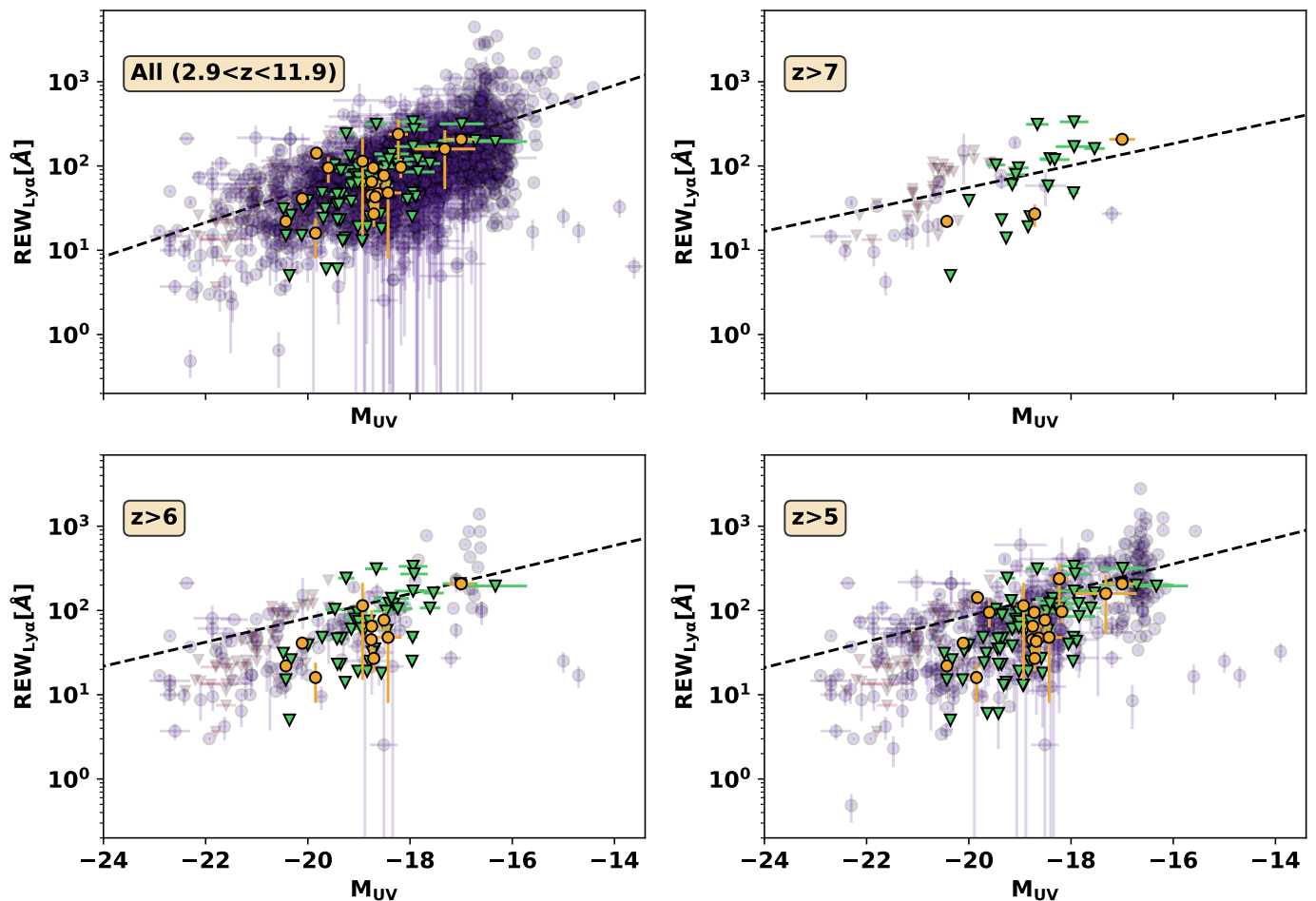


Fig. 6. Distribution of rest-frame Ly α equivalent widths as a function of M_{UV} for our sample (orange circles for detections and green triangles for 3σ upper limits) and from literature (purple circles for detections and red triangles for 3σ upper limits). An illustrative fit to the detections is shown by the black dashed line. See Appendix C for details of literature sample.

have hinted at a steep increase in $X_{Ly\alpha}$ between $z = 7 - 6$, with a more shallow drop off between $z = 6 - 4$. Since the JADES sample contains fainter galaxies (see Figure 5), we are instead able to focus on fainter galaxies ($M_{UV} > -20.25$).

We first divide our sample of galaxies into discrete redshift bins and calculate effective sample sizes by summing their completeness values (Section 3.5). The Ly α fraction is then found by dividing the number of galaxies in the redshift bin who meet the REW limit by the effective sample size (e.g., Caruana et al. 2012). This is repeated for three cuts on $REW_{Ly\alpha}$ ($> 25\text{\AA}$, $> 50\text{\AA}$, or $> 75\text{\AA}$), and we compare them to observed fractions from literature for galaxies fainter than $M_{UV} > -20.25$ (Stark et al. 2010, 2011; Ono et al. 2012; Schenker et al. 2012, 2014; Pentericci et al. 2014, 2018; see Figure 7).

For galaxies with $-20.25 < M_{UV} < -18.75$, previous studies have shown that the fraction for $EW > 25\text{\AA}$ increases from $z = 7$ to $z = 6$ with evidence for a decrease to $z = 4$, presumably due to the onset of IGM neutrality. Due to the low completeness of our sample at 25\AA (see Section 3.5), we are not able to place tight constraints on $X_{Ly\alpha}$ in this REW regime. Despite this, our estimates are in agreement with previous findings. The higher completeness at $REW > 50\text{\AA}$ and $REW > 75\text{\AA}$ results in agreement with previous results.

Overall, our sample supports a rise in the Ly α fraction between $z = 7$ and $z = 6$, as seen in previous studies. Since JADES

is ongoing, future investigations will include more data and yield tighter constraints on the evolution of this quantity. Even with our current data, we are able to constrain the IGM neutral fraction, as seen in the next subsection.

4.4. Constraints on neutral fraction

The observed Ly α fraction of galaxies for a given redshift, M_{UV} bin, and $REW_{Ly\alpha}$ limit provides valuable information on the neutral fraction of the IGM (X_{HI}). This is due to the fact that the evolution of $X_{Ly\alpha}(z \lesssim 6)$ is dependent only on galaxy properties, while at $z \gtrsim 6$ it is also dependent on the properties of IGM transmission. Some studies compared observed $X_{Ly\alpha}(z \sim 7)$ with the fraction expected from simulations, resulting in a range of estimates for $X_{HI}(z = 7)$: $\lesssim 0.3$ (Stark et al. 2010), ~ 0.5 (Caruana et al. 2014), $\gtrsim 0.51$ (Pentericci et al. 2014), $\sim 0.6 - 0.9$ (Ono et al. 2012), $\lesssim 0.7$ (Furusawa et al. 2016). This discrepancy may be partially explained by sample properties (e.g., difference in M_{UV} ranges and small sample sizes).

The conversion from $X_{Ly\alpha}$ to X_{HI} is nontrivial, and is dependent on the simulation used for comparison to observations. For example, the semi-numerical code DexM (Mesinger & Furlanetto 2007; Mesinger et al. 2011; Zahn et al. 2011) has been used by some works (e.g., Dijkstra et al. 2011; Pentericci et al. 2014) to create three-dimensional models of galaxy halos, determine

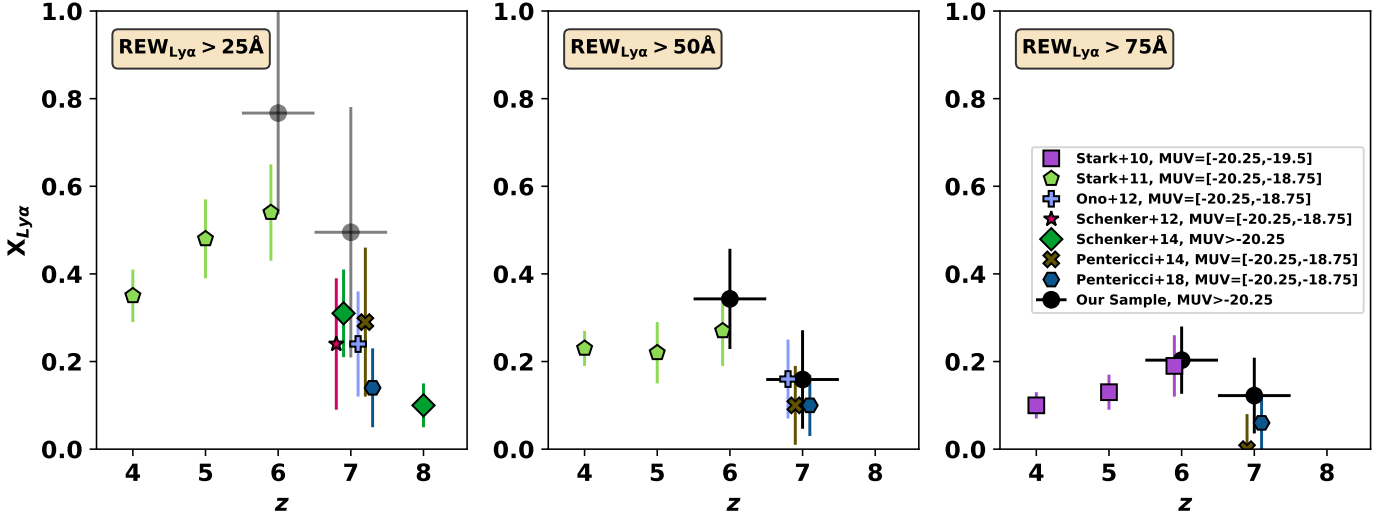


Fig. 7. Fraction of observed galaxies detected in Ly α emission with $\text{REW}_{\text{Ly}\alpha} > 25\text{\AA}$ (left), $\text{REW}_{\text{Ly}\alpha} > 50\text{\AA}$ (centre), and $\text{REW}_{\text{Ly}\alpha} > 75\text{\AA}$ (right). Derived fractions from literature are shown by coloured markers. For the central panel, note that Stark et al. (2011) and Ono et al. (2012) used a REW limit of $> 55\text{\AA}$. The fractions derived using only the observed JADES galaxies are shown by black points. Our $\text{REW} > 25\text{\AA}$ values (grey) are likely affected by low completeness.

how they ionise their surroundings, and characterise their redshift evolution. The outputs of this process (e.g., $X_{\text{Ly}\alpha}$) may then be compared to observations.

While an updated simulation is beyond the scope of this work, we may use our $X_{\text{Ly}\alpha}(\text{REW}_{\text{Ly}\alpha})$ values at $z \sim 7$ to generate a cumulative distribution Function (CDF) of $\text{REW}_{\text{Ly}\alpha}$, and compare this to model outputs of Pentericci et al. (2014). This model is appropriate for galaxies with $-20.25 < M_{\text{UV}} < -18.75$ and assumes $N_{\text{HI}} = 10^{20} \text{ cm}^{-2}$ and a wind speed of 200 km s^{-1} , but with a variable neutral fraction. It is based on the assumption that the Ly α CDF at $z = 6$ and $z = 7$ are intrinsically the same, but are observed to differ because of neutral IGM attenuation at $z = 7$. As seen in Figure 8, higher values of X_{HI} result in less Ly α transmission, and thus a steeper CDF. Literature values (Ono et al. 2012; Schenker et al. 2012; Pentericci et al. 2014, 2018) appear to argue for a value of $X_{\text{HI}} \sim 0.5 - 0.9$.

Our results (using a wide redshift bin of $6 < z < 8$) are in agreement with those of the previous studies (e.g., Mason et al. 2018), suggesting an approximate X_{HI} of $\sim 0.2 - 0.7$. Note that our $P(\text{REW} > 25\text{\AA})$ point is influenced by poor completeness, and thus does not provide a constraint. We note that this M_{UV} range is not optimised for our sample, and a future work will investigate how the redshift evolution ($z = 8 - 6$) of $P(> \text{REW})$ for $-20.4 < M_{\text{UV}} < -16$ galaxies may be used to constrain $X_{\text{HI}}(z)$.

The X_{HI} range of our analysis agrees with previous analyses that use the $\text{REW}_{\text{Ly}\alpha}$ cumulative distribution (e.g., Schenker et al. 2014; Pentericci et al. 2014, 2018) as well as simulations (e.g., Mason et al. 2018). This suggests that our estimates of $P(> \text{REW})$ have not been underestimated due to the NIRSspec MSA shutters ($0.2'' \sim 1 \text{ kpc}$ at $z \sim 7$) missing Ly α flux from extended halos, as noted by Jung et al. (2023). In this previous study, $F_{\text{Ly}\alpha, \text{MSA}}$ for one observed source was only 20% of the value as derived by MOSFIRE observations. On the other hand, Tang et al. (2023) found agreement between MSA- and ground-based estimates of $F_{\text{Ly}\alpha}$ for four $z \sim 7 - 9$ galaxies (but with large uncertainties for two sources). In addition, large Ly α halos are commonly seen at low- z , but will not have time to evolve for high-redshift sources. So while slit losses are unlikely to affect

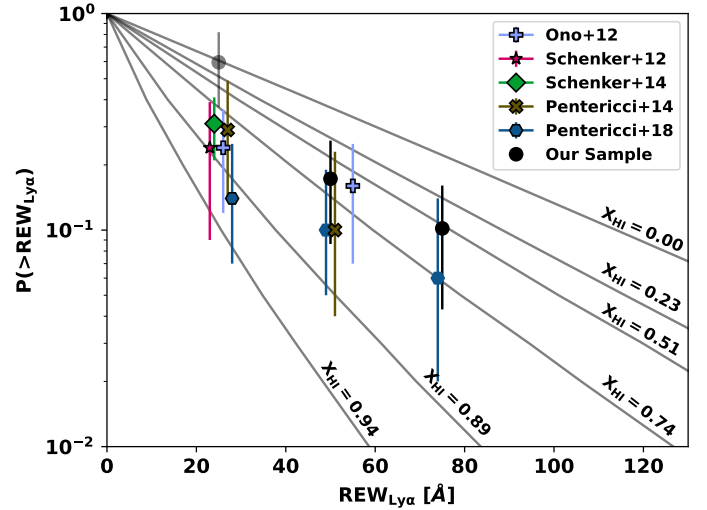


Fig. 8. Cumulative distribution for Ly α rest REW for UV-faint ($-20.25 < M_{\text{UV}} < -18.75$) galaxies at $z \sim 7$. Each solid line shows the expected distribution for a model with $N_{\text{HI}} = 10^{20} \text{ cm}^{-2}$ and a wind speed of 200 km s^{-1} , but with a different neutral fraction (Pentericci et al. 2014). Estimates from literature (Ono et al. 2012; Schenker et al. 2012, 2014; Pentericci et al. 2014, 2018) are shifted by 1\AA for visibility. Our $P(\text{REW} > 25\text{\AA})$ point (grey) is likely affected by low completeness.

our results, this effect may be further investigated by performing NIRSspec/IFU (field of view $3'' \times 3''$) observations of representative sources, or forward modelling the slit losses in simulations.

5. Conclusions

In this work, we present the first constraints on Ly α emission using JWST/NIRSspec MSA R100 spectra from the JADES survey. The increased sensitivity of this instrument enables deeper investigations of faint galaxies in the early Universe. Our sample consists of 84 galaxies at $z > 5.6$, each with secure spectroscopic redshifts (Bunker et al. 2023a). While the sample is

concentrated at $5.6 \lesssim z \lesssim 7.5$, we include sources up to $z \sim 12$. In addition, the $M_{UV} \sim -19.5$ to -17.5 range is well probed, but we include sources that are fainter ($M_{UV} \sim -16$) and brighter ($M_{UV} \sim -20.4$)

By fitting each spectrum with a line and/or continuum model, accounting for the spectral dispersion, and comparing the relative goodness of fit values, we find that 17 sources at $z \sim 5.6-8.0$ show evidence for Ly α emission in R100. The strong continuum of each source enables us to estimate the continuum flux (and M_{UV}) at the Ly α wavelength directly from the spectra. We derive Ly α rest-frame equivalent widths for each source.

We build a large comparison sample from literature of galaxies with estimates of spectroscopic redshifts, M_{UV} , and $REW_{Ly\alpha}$. By combining the JADES and literature samples, we find that the reported positive correlation between M_{UV} and $REW_{Ly\alpha}$ is supported for galaxies in multiple redshift bins, but the observed correlation in our data may be caused by sensitivity effects.

Next, we calculate the redshift evolution of the Ly α fraction ($X_{Ly\alpha}$) in bins of $REW_{Ly\alpha}$. Due to the faintness of the JADES sample ($M_{UV} \gtrsim -20.4$), we are able to place constraints on the poorly studied faint, high-redshift ($z \sim 6-7$) evolution of this fraction: a shallow increase from $z = 7$ to $z = 6$ for $REW > 50\text{\AA}$ and $REW > 75\text{\AA}$.

The distribution of $REW_{Ly\alpha}$ values was then used to place a constraint on the neutral fraction (X_{HI}) at $z \sim 7$ using the model of Pentericci et al. (2014). Our results indicate $X_{HI} \sim 0.2-0.7$, which is in agreement with previous studies.

The JADES survey is still ongoing, so this dataset will expand with time. In addition, many sources feature higher resolution R1000 spectra, which enable further science cases such as Ly α velocity offset and line asymmetry analysis, damping wing modelling, and environments of Ly α emitters. Combined, these analyses will reveal the details of reionization in unprecedented detail.

Acknowledgements

G CJ, A JB, A S, A J C, and J C acknowledge funding from the ‘‘FirstGalaxies’’ Advanced Grant from the European Research Council (ERC) under the European Union’s Horizon 2020 research and innovation programme (Grant agreement No. 789056). J W, R M, W M B, T J L, L S, and J S acknowledge support by the Science and Technology Facilities Council (STFC) and by the ERC through Advanced Grant 695671 ‘‘QUENCH’’. J W also acknowledges funding from the Fondation MERAC. R M also acknowledges funding from the UKRI Frontier Research grant RISEandFALL and from a research professorship from the Royal Society. S A acknowledges support from Grant PID2021-127718NB-I00 funded by the Spanish Ministry of Science and Innovation/State Agency of Research (MICIN/AEI/10.13039/501100011033). R B acknowledges support from an STFC Ernest Rutherford Fellowship (ST/T003596/1). This research is supported in part by the Australian Research Council Centre of Excellence for All Sky Astrophysics in 3 Dimensions (ASTRO 3D), through project number CE170100013. S C acknowledges support by European Union’s HE ERC Starting Grant No. 101040227 - WINGS. E C L acknowledges support of an STFC Webb Fellowship (ST/W001438/1). D J E, B D J, and B E R acknowledge a JWST/NIRCam contract to the University of Arizona NAS5-02015. D J E is supported as a Simons Investigator. Funding for this research was provided by the Johns Hopkins University, Institute for Data Intensive Engineering and Science (IDIES). R S acknowledges support from a STFC Ernest

Rutherford Fellowship (ST/S004831/1). H U gratefully acknowledges support by the Isaac Newton Trust and by the Kavli Foundation through a Newton-Kavli Junior Fellowship. The research of C C W is supported by NOIRLab, which is managed by the Association of Universities for Research in Astronomy (AURA) under a cooperative agreement with the National Science Foundation. G C J would like to thank C. Witten and N. Laporte for valuable insight into the sample. We thank the anonymous referee for constructive feedback that has enhanced this work.

References

- Böker, T., Beck, T. L., Birkmann, S. M., et al. 2023, *PASP*, 135, 038001
- Bolan, P., Lemaux, B. C., Mason, C., et al. 2022, *MNRAS*, 517, 3263
- Bouwens, R. J., Illingworth, G. D., Oesch, P. A., et al. 2015, *ApJ*, 803, 34
- Bunker, A. J., Cameron, A. J., Curtis-Lake, E., et al. 2023a, arXiv e-prints, arXiv:2306.02467
- Bunker, A. J., NIRSPEC Instrument Science Team, & JAESs Collaboration. 2020, in *Uncovering Early Galaxy Evolution in the ALMA and JWST Era*, ed. E. da Cunha, J. Hodge, J. Afonso, L. Pentericci, & D. Sobral, Vol. 352, 342–346
- Bunker, A. J., Saxena, A., Cameron, A. J., et al. 2023b, *A&A*, 677, A88
- Bunker, A. J., Stanway, E. R., Ellis, R. S., & McMahon, R. G. 2004, *MNRAS*, 355, 374
- Cai, Z., Fan, X., Yang, Y., et al. 2017, *ApJ*, 837, 71
- Cain, C., D’Aloisio, A., Gangolli, N., & Becker, G. D. 2021, *ApJ*, 917, L37
- Caruana, J., Bunker, A. J., Wilkins, S. M., et al. 2012, *MNRAS*, 427, 3055
- Caruana, J., Bunker, A. J., Wilkins, S. M., et al. 2014, *MNRAS*, 443, 2831
- Cassata, P., Tasca, L. A. M., Le Fèvre, O., et al. 2015, *A&A*, 573, A24
- Christenson, H. M., Becker, G. D., Furlanetto, S. R., et al. 2021, *ApJ*, 923, 87
- Cuby, J. G., Le Fèvre, O., McCracken, H., et al. 2003, *A&A*, 405, L19
- Curtis-Lake, E., Carniani, S., Cameron, A., et al. 2023, *Nature Astronomy*, 7, 622
- Curtis-Lake, E., McLure, R. J., Pearce, H. J., et al. 2012, *MNRAS*, 422, 1425
- Dey, A., Bian, C., Soifer, B. T., et al. 2005, *ApJ*, 629, 654
- Dickinson, M., Giavalisco, M., & GOODS Team. 2003, in *The Mass of Galaxies at Low and High Redshift*, ed. R. Bender & A. Renzini, 324
- Dijkstra, M., Mesinger, A., & Wyithe, J. S. B. 2011, *MNRAS*, 414, 2139
- Dijkstra, M., & Wyithe, J. S. B. 2010, *MNRAS*, 408, 352
- Drake, A. B., Neeleman, M., Venemans, B. P., et al. 2022, *ApJ*, 929, 86
- Eisenstein, D. J., Willott, C., Alberts, S., et al. 2023, arXiv e-prints, arXiv:2306.02465
- Endsley, R., Stark, D. P., Bouwens, R. J., et al. 2022, *MNRAS*, 517, 5642
- Endsley, R., Stark, D. P., Chevallard, J., & Charlot, S. 2021, *MNRAS*, 500, 5229
- Erb, D. K., Steidel, C. C., Trainor, R. F., et al. 2014, *ApJ*, 795, 33
- Fan, X., Bañados, E., & Simcoe, R. A. 2023, *ARA&A*, 61, 373
- Fan, X., Strauss, M. A., Becker, R. H., et al. 2006, *AJ*, 132, 117
- Ferruit, P., Jakobsen, P., Giardino, G., et al. 2022, *A&A*, 661, A81
- Fontana, A., Vanzella, E., Pentericci, L., et al. 2010, *ApJ*, 725, L205
- Fujimoto, S., Wang, B., Weaver, J., et al. 2023, arXiv e-prints, arXiv:2308.11609
- Fuller, S., Lemaux, B. C., Bradač, M., et al. 2020, *ApJ*, 896, 156
- Furusawa, H., Kashikawa, N., Kobayashi, M. A. R., et al. 2016, *ApJ*, 822, 46
- Gnedin, N. Y. 2000, *ApJ*, 535, 530
- Guo, Y., Bacon, R., Wisotzki, L., et al. 2023, arXiv e-prints, arXiv:2309.06311
- Harikane, Y., Ouchi, M., Ono, Y., et al. 2016, *ApJ*, 821, 123
- Heintz, K. E., Watson, D., Brammer, G., et al. 2023, arXiv e-prints, arXiv:2306.00647
- Hoag, A., Bradač, M., Huang, K., et al. 2019, *ApJ*, 878, 12
- Hutchison, T. A., Papovich, C., Finkelstein, S. L., et al. 2019, *ApJ*, 879, 70
- Iye, M., Ota, K., Kashikawa, N., et al. 2006, *Nature*, 443, 186
- Jakobsen, P., Ferruit, P., Alves de Oliveira, C., et al. 2022, *A&A*, 661, A80
- Jung, I., Finkelstein, S. L., Arrabal Haro, P., et al. 2023, arXiv e-prints, arXiv:2304.05385
- Jung, I., Finkelstein, S. L., Larson, R. L., et al. 2022, arXiv e-prints, arXiv:2212.09850
- Kerutt, J., Wisotzki, L., Verhamme, A., et al. 2022, *A&A*, 659, A183
- Kikuta, S., Matsuda, Y., Inoue, S., et al. 2023, *ApJ*, 947, 75
- Larson, R. L., Finkelstein, S. L., Hutchison, T. A., et al. 2022, *ApJ*, 930, 104
- Li, J., Emonts, B. H. C., Cai, Z., et al. 2021, *ApJ*, 922, L29
- Marchi, F., Pentericci, L., Guaita, L., et al. 2019, *A&A*, 631, A19
- Mason, C. A., Fontana, A., Treu, T., et al. 2019, *MNRAS*, 485, 3947
- Mason, C. A. & Gronke, M. 2020, *MNRAS*, 499, 1395
- Mason, C. A., Treu, T., Dijkstra, M., et al. 2018, *ApJ*, 856, 2
- Matthee, J., Naidu, R. P., Pezzulli, G., et al. 2022, *MNRAS*, 512, 5960
- Matthee, J., Sobral, D., Boogaard, L. A., et al. 2019, *ApJ*, 881, 124
- Mesinger, A. & Furlanetto, S. 2007, *ApJ*, 669, 663
- Mesinger, A., Furlanetto, S., & Cen, R. 2011, *MNRAS*, 411, 955

- Mesinger, A. & Furlanetto, S. R. 2008, *MNRAS*, 385, 1348
- Miralda-Escudé, J. 1998, *ApJ*, 501, 15
- Morales, A. M., Mason, C. A., Bruton, S., et al. 2021, *ApJ*, 919, 120
- Mortlock, D. 2016, in *Astrophysics and Space Science Library*, Vol. 423, Understanding the Epoch of Cosmic Reionization: Challenges and Progress, ed. A. Mesinger, 187
- Naidu, R. P., Tacchella, S., Mason, C. A., et al. 2020, *ApJ*, 892, 109
- Newville, M., Stensitzki, T., Allen, D. B., & Ingargiola, A. 2014, LMFIT: Non-Linear Least-Square Minimization and Curve-Fitting for Python
- Oesch, P. A., van Dokkum, P. G., Illingworth, G. D., et al. 2015, *ApJ*, 804, L30
- Oke, J. B. & Gunn, J. E. 1983, *ApJ*, 266, 713
- Ono, Y., Ouchi, M., Mobasher, B., et al. 2012, *ApJ*, 744, 83
- Pentericci, L., Vanzella, E., Castellano, M., et al. 2018, *A&A*, 619, A147
- Pentericci, L., Vanzella, E., Fontana, A., et al. 2014, *ApJ*, 793, 113
- Prieto-Lyon, G., Mason, C., Mascia, S., et al. 2023, *ApJ*, 956, 136
- Reuland, M., van Breugel, W., Röttgering, H., et al. 2003, *ApJ*, 592, 755
- Richard, J., Claeysens, A., Lagattuta, D., et al. 2021, *A&A*, 646, A83
- Rieke, M. J., Kelly, D. M., Misselt, K., et al. 2023, *PASP*, 135, 028001
- Roberts-Borsani, G. W., Bouwens, R. J., Oesch, P. A., et al. 2016, *ApJ*, 823, 143
- Roy, N., Henry, A., Treu, T., et al. 2023, *ApJ*, 952, L14
- Saxena, A., Bunker, A. J., Jones, G. C., et al. 2023, *arXiv e-prints*, arXiv:2306.04536
- Schenker, M. A., Ellis, R. S., Konidaris, N. P., & Stark, D. P. 2014, *ApJ*, 795, 20
- Schenker, M. A., Stark, D. P., Ellis, R. S., et al. 2012, *ApJ*, 744, 179
- Shibuya, T., Ouchi, M., Harikane, Y., et al. 2018, *PASJ*, 70, S15
- Song, M., Finkelstein, S. L., Livermore, R. C., et al. 2016, *ApJ*, 826, 113
- Stark, D. P., Ellis, R. S., Charlot, S., et al. 2017, *MNRAS*, 464, 469
- Stark, D. P., Ellis, R. S., Chiu, K., Ouchi, M., & Bunker, A. 2010, *MNRAS*, 408, 1628
- Stark, D. P., Ellis, R. S., & Ouchi, M. 2011, *ApJ*, 728, L2
- Steidel, C. C., Adelberger, K. L., Shapley, A. E., et al. 2000, *ApJ*, 532, 170
- Tang, M., Stark, D. P., Chen, Z., et al. 2023, *MNRAS*, 526, 1657
- Taylor, J. & Lidz, A. 2014, *MNRAS*, 437, 2542
- Thai, T. T., Tuan-Anh, P., Pello, R., et al. 2023, *A&A*, 678, A139
- Tilvi, V., Malhotra, S., Rhoads, J. E., et al. 2020, *ApJ*, 891, L10
- Umeda, H., Ouchi, M., Nakajima, K., et al. 2023, *arXiv e-prints*, arXiv:2306.00487
- Vanzella, E., Pentericci, L., Fontana, A., et al. 2011, *ApJ*, 730, L35
- Villanueva-Domingo, P., Gariazzo, S., Gnedin, N. Y., & Mena, O. 2018, *J. Cosmology Astropart. Phys.*, 2018, 024
- Witstok, J., Smit, R., Saxena, A., et al. 2023, *arXiv e-prints*, arXiv:2306.04627
- Yoshioka, T., Kashikawa, N., Inoue, A. K., et al. 2022, *ApJ*, 927, 32
- Zahn, O., Mesinger, A., McQuinn, M., et al. 2011, *MNRAS*, 414, 727
- Zhang, H., Cai, Z., Liang, Y., et al. 2023, *arXiv e-prints*, arXiv:2301.07358
- Zhu, Y., Becker, G. D., Bosman, S. E. I., et al. 2022, *ApJ*, 932, 76
- Zitrin, A., Labbé, I., Belli, S., et al. 2015, *ApJ*, 810, L12
- ¹⁴ European Southern Observatory, Karl-Schwarzschild-Strasse 2, 85748 Garching, Germany
- ¹⁵ Centre for Astrophysics Research, Department of Physics, Astronomy and Mathematics, University of Hertfordshire, Hatfield AL10 9AB, UK
- ¹⁶ Center for Astrophysics | Harvard & Smithsonian, 60 Garden St., Cambridge, MA 02138, USA
- ¹⁷ Department of Physics and Astronomy, The Johns Hopkins University, 3400 N. Charles St., Baltimore, MD 21218, USA
- ¹⁸ AURA for European Space Agency, Space Telescope Science Institute, 3700 San Martin Drive. Baltimore, MD, 21210, USA
- ¹⁹ Department of Astronomy, University of Wisconsin-Madison, 475 N. Charter St., Madison, WI 53706 USA
- ²⁰ Max-Planck-Institut für Astronomie, Königstuhl 17, D-69117, Heidelberg, Germany
- ²¹ Department of Astronomy and Astrophysics, University of California, Santa Cruz, 1156 High Street, Santa Cruz, CA 95064, USA
- ²² Astrophysics Research Institute, Liverpool John Moores University, 146 Brownlow Hill, Liverpool L3 5RF, UK
- ²³ NSF's National Optical-Infrared Astronomy Research Laboratory, 950 North Cherry Avenue, Tucson, AZ 85719, USA
- ²⁴ NRC Herzberg, 5071 West Saanich Rd, Victoria, BC V9E 2E7, Canada

¹ Department of Physics, University of Oxford, Denys Wilkinson Building, Keble Road, Oxford OX1 3RH, UK

² Department of Physics and Astronomy, University College London, Gower Street, London WC1E 6BT, UK

³ Kavli Institute for Cosmology, University of Cambridge, Madingley Road, Cambridge CB3 0HA, UK

⁴ Cavendish Laboratory, University of Cambridge, 19 JJ Thomson Avenue, Cambridge CB3 0HE, UK

⁵ Steward Observatory, University of Arizona, 933 N. Cherry Ave., Tucson, AZ 85721 USA

⁶ Centro de Astrobiología (CAB), CSIC-INTA, Cra. de Ajalvir Km. 4, 28850- Torrejón de Ardoz, Madrid, Spain

⁷ European Space Agency (ESA), European Space Astronomy Centre (ESAC), Camino Bajo del Castillo s/n, 28692 Villanueva de la Cañada, Madrid, Spain

⁸ European Space Agency, ESA/ESTEC, Keplerlaan 1, 2201 AZ Noordwijk, NL

⁹ Jodrell Bank Centre for Astrophysics, Department of Physics and Astronomy, School of Natural Sciences, The University of Manchester, Manchester, M13 9PL, UK

¹⁰ School of Physics, University of Melbourne, Parkville 3010, VIC, Australia

¹¹ ARC Centre of Excellence for All Sky Astrophysics in 3 Dimensions (ASTRO 3D), Australia

¹² Scuola Normale Superiore, Piazza dei Cavalieri 7, I-56126 Pisa, Italy

¹³ Sorbonne Université, CNRS, UMR 7095, Institut d'Astrophysique de Paris, 98 bis bd Arago, 75014 Paris, France

Appendix A: Damping wing in R100

In this work, we assume that the Ly α break may be approximated by a step function. To test whether this is appropriate for our R100 spectra, we consider the wavelength-dependent damping wing optical depth formalism of Miralda-Escudé (1998) for a source at redshift z_s :

$$\tau(\Delta\lambda) = \frac{\tau_o R_\alpha}{\pi} (1 + \delta)^{3/2} [F(x_2) - F(x_1)] \quad (\text{A.1})$$

where $\Delta\lambda$ is the wavelength offset from the redshifted centroid of Ly α (λ_α), $\delta \equiv \Delta\lambda/[\lambda_\alpha(1 + z_s)]$, and we assume $\tau_o = \tau_{GP} = (7.16 \times 10^5) \times \left(\frac{1+z_s}{10}\right)^{3/2}$ and $R_\alpha = 2.0136 \times 10^{-8}$ from Mesinger & Furlanetto (2008). $F(x)$ is given as:

$$F(x) = \frac{x^{9/2}}{1-x} + \frac{9x^{7/2}}{7} + \frac{9x^{5/2}}{5} + 3x^{3/2} + 9x^{1/2} - \frac{9}{2} \log \frac{1+x^{1/2}}{1-x^{1/2}} \quad (\text{A.2})$$

with $x_1 = (1+z_n)/[(1+z_s)(1+\delta)]$ and $x_2 = 1/(1+\delta)$ where z_n is the redshift where absorption by the IGM is assumed to be negligible (we use the standard assumption of $z_n = 6$; e.g., Mortlock 2016; Fan et al. 2023). We note that in this form, the model assumes a uniform X_{HI} between $z_n < z < z_s$ (here assumed to be unity) and a no IGM absorption below $z < z_n$.

As z_s approaches z_n from high values, the damping wing begins to approximate a step function. For sources below z_n (which includes most sources in our sample), the IGM is expected to have little effect, and a step function is thus appropriate. But for sources above z_n , it is possible that the damping wing will have an effect.

To investigate this, the optical depth model is used to create a transmission spectrum for a source at $z_s = 10$, using the same wavelength grid as our R100 spectra (see solid lines of Figure A.1). To account for the instrumental dispersion, this model is convolved with a Gaussian with $\sigma = \sigma_R$ (see Section 3.1; dashed lines of Figure A.1).

For $\lambda \gg \lambda_{Ly\alpha}$ or $\lambda \ll \lambda_{Ly\alpha}$, the two convolved curves are similar (i.e., either 0 or unity). But in this case of a $z = 10$ source, the curves differ at $\lambda \sim \lambda_{Ly\alpha}$, with a discrepancy of up to $\sim 20\%$. This strong difference may be detected for some sources, and will be used in future works to place constraints on the proximity zones and IGM neutral fraction of $z > 8$ sources in JADES (e.g., Jakobsen et al. in prep). Indeed, multiple studies have now used JWST/NIRSpec observations to constrain the Ly α damping wing (e.g., Fujimoto et al. 2023; Heintz et al. 2023; Umeda et al. 2023).

Throughout this work, we assume that the transmission function for galaxies in our sample is a simple step function (i.e., 100% transmission redwards of $\lambda_{Ly\alpha}$). In reality, damping wings will affect all of the $z \gtrsim 8$ sources, resulting in low transmission at $\lambda_{Ly\alpha}$ and thus making it more difficult to detect Ly α emission. For the six $z > 8$ sources in our sample (none of which are detected in Ly α emission), we note that this is not accounted for in our $REW_{Ly\alpha}$ upper limits, so these may be slightly underestimated. But a full treatment of the damping wing effect is beyond the scope of this paper and will be fully explored in a future analysis.

Appendix B: M_{UV} Derivation

Due to the high quality of the NIRSpec spectra, we are able to derive $M_{1500\text{\AA}}$ absolute magnitudes (M_{UV}) directly from the observed data. First, the observed data are shifted from the observed to rest frame by multiplying all flux values (i.e., f_λ) by

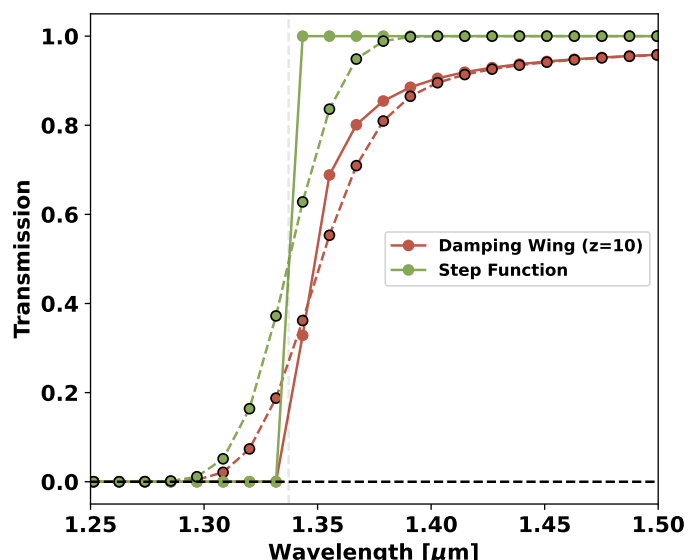


Fig. A.1. Transmission models of a damping wing (brown lines) and a step function (green lines) for a $z = 10$ source. We include the intrinsic model, regridded to match our R100 observations (solid lines), and the dispersed version of this model (dashed lines). The Ly α wavelength is shown by a faint vertical line.

$1 + z$ and dividing all wavelength values by the same factor. The rest-frame f_λ values are converted to a f_v :

$$f_v = f_\lambda \lambda^2 / c \quad (\text{B.1})$$

where c is the speed of light. We collect and average all f_v values that lie between 1400–1600 Å (rest-frame), and use this average value (\bar{f}_v) to derive an apparent AB magnitude (Oke & Gunn 1983):

$$m_{1500} = -2.5 \log_{10}(\bar{f}_v) - 48.60 \quad (\text{B.2})$$

which is converted to an absolute magnitude:

$$M_{UV} = m_{1500} - 5 \log_{10}(D_L [Mpc]) - 25 \quad (\text{B.3})$$

An error is estimated by calculating the root mean square noise level of the f_v values between 1400–1600 Å from the error spectrum and perturbing \bar{f}_v by this value.

Appendix C: Comparison data

As one of the brightest emission lines for star-forming galaxies at high-redshift, Ly α has been studied in numerous galaxies over the past decades. While the subset of JADES that we analyse in this work offers the opportunity to explore the Ly α properties of galaxies between $z \sim 5-11$, our conclusions are strengthened by the addition of archival data. Here, we collect a large literature sample of galaxies with reported spatial positions, spectroscopic redshifts, Ly α equivalent widths from spectral observations, and M_{UV} values. Unless otherwise stated, $z_{sys} = z_{Ly\alpha}$ and $M_{UV} = M_{1500}$. The details of our comparison sample are given below, and we present a full machine readable table³. To avoid repeated galaxies, we search for entries within 0.25'' of each other and exclude the older measurement.

³ (See published version for permanent CDS link) https://drive.google.com/file/d/1idNB3hEUXLCg4JXPQjv4SjS9KtZdI_ds/view?usp=sharing

Followup spectroscopy of bright Ly α emitters (LAEs) discovered in the Systematic Identification of LAEs for Visible Exploration and Reionization Research Using Subaru HSC (SILVERRUSH) with a variety of ground-based telescopes resulted in numerous detections (Shibuya et al. 2018). The continuum level underlying Ly α was found by extrapolating from red filters ($\beta = -2$), while M_{UV} was estimated from the observed spectra.

We also include the large survey CANDELSz7 (Pentericci et al. 2018), a large program that observed star-forming galaxies at $z \sim 6$ and $z \sim 7$ in the GOODS-South, UDS, and COSMOS fields with the VLT/FORS2 spectrograph. We include all galaxies with good quality flags (i.e., A, A/B, and B) and Ly α flux estimates. M_{UV} values are estimated using fits to CANDELS photometry, while the REW is derived by fitting the observed spectra. Six sources are also observed with MUSE by Kerutt et al. (2022), so they are not included.

Next, we include the results of studies that used Keck/MOSFIRE. Jung et al. (2022) observed eight $z \sim 7 - 8$ galaxies in CANDELS EGS and used an asymmetric Gaussian to fit the Ly α emission. We exclude one source that lacks a spectroscopic redshift and a number of galaxies with only upper limits on REW $_{Ly\alpha}$. Four galaxies in this sample likely re-observed in Tang et al. (2023), so they are also excluded. While Tilvi et al. (2020) observed three galaxies in group at $z = 7.7$, we take the one source with M_{UV} calculated by Tang et al. (2023), or z8_5 (EGS-zs8-1 in Oesch et al. 2015). Song et al. (2016) detected one galaxy in Ly α emission (z7_GSD_3811), whose emission was fit with an asymmetric profile. Hoag et al. (2019) detected Ly α emission from two galaxies that are strongly lensed by galaxy clusters. Values are magnification-corrected, and equivalent width is calculated by dividing the line flux by HST WFC3/F160W continuum flux.

Keck/DEIMOS spectroscopy by Ono et al. (2012) resulted in line detections for three $z \sim 7$ galaxies in the SDF and GOODS-North. The continuum properties were derived from a fit to the photometry. Further Keck/DEIMOS observations revealed 36 LAEs (Fuller et al. 2020). Note that SDF-63544 is also known as IOK-1 (e.g., Iye et al. 2006). Additional Keck observations resulted in three detections of Ly α with the spectrographs LRIS and NIRSPEC (Schenker et al. 2012), where the continuum was estimated by extrapolating a power-law model ($\beta = -2$) from a red filter.

Two works used the VLT/FORS2 spectrograph (Cuby et al. 2003; Vanzella et al. 2011). For these, we take M_{UV} from the compilation of Matthee et al. (2019). Additionally, the GMOS spectrographs on the 8.2m Gemini Telescopes were used to observe one target. The resulting spectra were fit with templates, resulting in a Ly α REW and M_{1350} .

The MMT/Binospec spectrograph was used to observe eight UV-bright ($M_{UV} \sim -22$) galaxies at $z \sim 7$ selected from the ALMA REBELS survey (Endsley et al. 2022). Red bands were used to estimate the Ly α continuum, while $M_{UV} \equiv M_{1600}$.

VLT/MUSE features a bluer spectral range ($0.465 - 0.930 \mu\text{m}^4$) with respect to the JWST/NIRSpec PRISM/CLEAR filter/disperser combination ($0.6 - 5.3 \mu\text{m}$), allowing it to probe Ly α to lower redshifts ($z \sim 2.8 - 6.7$). Through the MUSE-WIDE and MUSE-DEEP surveys, Kerutt et al. (2022) present the Ly α equivalent widths for 1920 galaxies over the full redshift range accessible to MUSE. The continuum level at $\lambda_{Ly\alpha}$ is estimated from photometry, while Ly α is measured from each MUSE data cube.

We also include 10 galaxies in the Abell 2744 cluster from the recent work of Prieto-Lyon et al. (2023), who analysed data from the GLASS-JWST Early Release Science program. M_{UV} values were derived from SED fits to HST and JWST photometry, while REW $_{Ly\alpha}$ is taken from the MUSE observations of Richard et al. (2021). The systemic redshift is derived from fits to optical lines as observed by JWST.

Finally, we include results from the recent work of Tang et al. (2023), who used the MSA of JWST/NIRSpec (R100 and R1000) to extract spectra and continuum estimates for ten sources. Four sources feature small spatial offsets ($< 0.1''$) and redshift differences ($\delta z \sim 0.25 - 0.35$) with sources observed with Keck/MOSFIRE by Tang et al. (2023). Since the redshift difference may be explained by a difference in methods (i.e., photometric vs. spectroscopic), we assume that these are the same galaxies. Here, $z_{sys} = z_{[OIII]5007}$. Ly α and continuum properties were extracted from the CEERS spectra and from photometry, respectively. The NIRSpec-based Ly α properties agree with ground-based REW measurements, suggesting the absence of calibration issues. A few of these sources were known by other names in previous studies: CEERS-1019 is EGSY8p7 (Zitrin et al. 2015), CEERS-1029 is EGS_z910_44164 (Larson et al. 2022), and CEERS-698 is EGS-zs8-2 (Roberts-Borsani et al. 2016).

Appendix D: REW- M_{UV} simulation

In Section 4.2, we found that the REW $_{Ly\alpha}$ and M_{UV} of our sample showed an apparent positive relation, such that more UV-faint galaxies featured larger Ly α equivalent widths. But since REW is a ratio of line flux to continuum flux, it is possible that this relation is influenced by the sensitivity limit of our sample and fitting method (i.e., we may miss Ly α -faint galaxies). In this Section, we test this possibility using a method similar to our completeness analysis (Section 3.5).

For each survey tier (Deep/HST, Medium/HST, Medium/JWST), we create 750 model spectra by sampling uniformly for several properties ($5.6 < z < 12.0$, $-20.4 < M_{UV} < -16.4$, spectral slope $-2 < n < 2$, $0.1 < F_R < 0.8$) and log-uniformly for Ly α equivalent width ($1 < \text{REW}_{Ly\alpha} < 750 \text{\AA}$). Gaussian noise is added to each model spectrum based on the corresponding mean error spectrum, and the resulting spectrum is fit with our routine.

In Figure D.1, we show the intrinsic distribution of REW vs M_{UV} in blue, and display the resulting best-fit values as red-outlined black circles. Upper limits on REW (3σ) are shown as downwards arrows. It is clear that we do not capture the full distribution, as galaxies in the lower-right corner (UV-faint and low-REW) are not able to be fit. From this test, it is clear that our sample and fitting approach may result in a false positive trend of REW with M_{UV} , due to sensitivity limits.

⁴ <https://www.eso.org/sci/facilities/paranal/instruments/muse/inst.html>

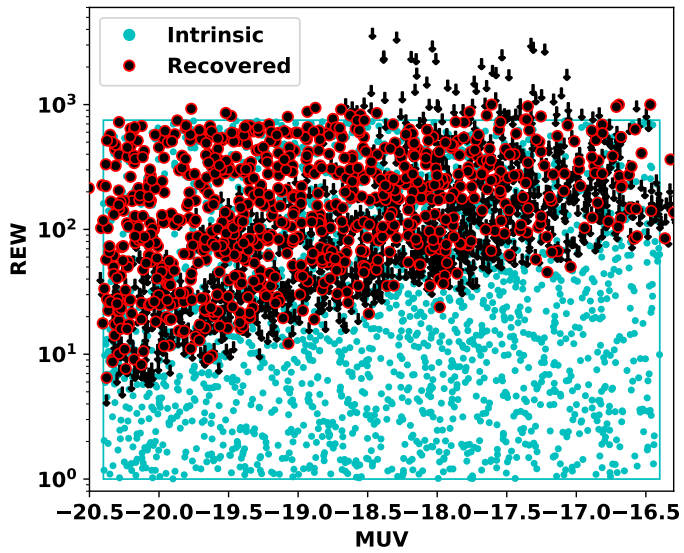


Fig. D.1. Results of fitting a sample of simulated galaxies. The intrinsic distribution of REW and M_{UV} for the simulated galaxies are shown as cyan circles, with a cyan rectangle outlining the region. The best-fit values and 3σ upper limits are shown as red-outlined circles and black arrows, respectively.